Influence of temperature-dependent shear viscosity on elliptic flow at backward and forward rapidities in ultrarelativistic heavy-ion collisions

E. Molnár,[1,2] H. Holopainen,[2] P. Huovinen,[2,3] and H. Niemi[4,5]

[1]*MTA-DE Particle Physics Research Group, H-4010 Debrecen, P.O. Box 105, Hungary*

[2]*Frankfurt Institute for Advanced Studies, Ruth-Moufang-Strasse 1, D-60438 Frankfurt am Main, Germany*

[3]*Institut für Theoretische Physik, Johann Wolfgang Goethe-Universität, Max-von-Laue-Strasse 1, D-60438 Frankfurt am Main, Germany*

[4]*Department of Physics, University of Jyväskylä, P.O. Box 35 (YFL), FI-40014 University of Jyväskylä, Finland*

[5]*Helsinki Institute of Physics, P.O. Box 64, FI-00014 University of Helsinki, Finland*

(Received 31 July 2014; revised manuscript received 12 September 2014; published 7 October 2014)

We explore the influence of a temperature-dependent shear viscosity over entropy density ratio η_s/s on the azimuthal anisotropies v_2 and v_4 of hadrons at various rapidities. We find that in Au + Au collisions at full Relativistic Heavy Ion Collider energy, $\sqrt{s_{\rm NN}} = 200$ GeV, the flow anisotropies are dominated by hadronic viscosity at all rapidities, whereas in Pb + Pb collisions at the Large Hadron Collider energy, $\sqrt{s_{\rm NN}} = 2760$ GeV, the flow coefficients are affected by the viscosity in both the plasma and hadronic phases at midrapidity, but the further away from midrapidity, the more dominant the hadronic viscosity becomes. We find that the centrality and rapidity dependence of the elliptic and quadrangular flows can help to distinguish different parametrizations of $(\eta_s/s)(T)$. We also find that at midrapidity the flow harmonics are almost independent of the decoupling criterion, but they show some sensitivity to the criterion at backward and forward rapidities.

DOI: 10.1103/PhysRevC.90.044904 PACS number(s): 25.75.Ld, 12.38.Mh, 24.10.Nz

I. INTRODUCTION

Determining the transport properties of the quark-gluon plasma (QGP) formed in ultrarelativistic nuclear collisions [1] is nowadays one of the main goals in high-energy nuclear physics. Fluid-dynamical models indicate a very low shear viscosity to entropy density ratio η_s/s,[1] when tuned to reproduce the azimuthal anisotropies of the transverse momentum distributions of observed hadrons. For recent reviews see, for example, Refs. [2–4]. The values favored by state-of-the-art calculations are in the vicinity of the conjectured lower limit for shear viscosity, $\eta_s/s = 1/(4\pi)$, based on the anti–de Sitter/conformal field theory (AdS/CFT) correspondence [5]. For example, the values found in Ref. [6] are $\eta_s/s = 0.12$ for collisions at the Relativistic Heavy-Ion Collider (RHIC) at Brookhaven National Laboratory and $\eta_s/s = 0.2$ at the Large Hadron Collider (LHC) at CERN.

The values quoted above were obtained by using a constant η_s/s ratio during the entire evolution of the system. For a physical system η_s/s depends at least on temperature [7] and on baryon density [8]. A constant value of η_s/s represents only an effective average over the entire space-time evolution of the system. The slightly larger effective η_s/s obtained for collisions at the LHC, i.e., at larger collision energy, thus may be interpreted as an indication of the temperature dependence of η_s/s [9,10]. Unfortunately, extracting the temperature dependence of η_s/s from the experimental data is a challenging problem.

In our previous works [11–13], we have studied the consequences of relaxing the assumption of a constant η_s/s. We found that the relevant temperature region where the shear viscosity affects the elliptic flow most varies with the collision energy. At the RHIC the most relevant region is around and below the QCD transition temperature, while for higher collision energies the temperature region above the transition becomes more and more important. To constrain the temperature dependence of η_s/s better, it would thus be necessary to find observables which are sensitive to the shear viscosity at different stages of the evolution of a single collision.

In this work we relax the assumption of boost invariance of our earlier works, solve the evolution equations numerically in all three dimensions, and study whether the azimuthal anisotropies have similar dependence on $(\eta_s/s)(T)$ at all rapidities. If not, the measurements of v_n at backward and forward rapidities could bring further constraints to $(\eta_s/s)(T)$.

We also approach the problem of extracting the temperature dependence of η_s/s in a fashion similar to that of Ref. [9]: We tune different parametrizations to reproduce the anisotropies at one collision energy and centrality and check whether anisotropies at different centralities, rapidities, and collision energies can distinguish between these parametrizations.

Furthermore, we check the sensitivity of our results to different decoupling criteria. To this end we carry out the calculations using a dynamical freeze-out criterion, i.e., freeze-out at constant Knudsen number [14–16], and compare the results to those obtained using the conventional freeze-out at constant temperature.

In the following we describe the structure and freeze-out in our (3+1)-dimensional dissipative fluid-dynamical model in Sec. II and the parameters in our calculations in Sec. III. Section IV contains the comparison of our results with experimental data, while in Secs. V and VI we discuss whether it is possible to distinguish the details of different parametrizations of $(\eta_s/s)(T)$, as well as the effects of a

[1]In this work η_s denotes the coefficient of shear viscosity, $\eta_{\rm ch}$ the pseudorapidity, and η the space-time rapidity.

dynamical freeze-out criterion. We summarize our results in Sec. VII.

Specific details of the fluid-dynamical equations are relegated to Appendix A. The numerical algorithm and details of our implementation and the numerical accuracy of our code are discussed in Appendices B, and C, respectively.

In this work we use natural units $\hbar = c = k = 1$.

II. FLUID DYNAMICS

A. Equations of motion

Relativistic fluid dynamics corresponds to the local conservation of energy-momentum and net-charge currents (if any),

$$\partial_\mu T^{\mu\nu} = 0, \quad \partial_\mu N_i^\mu = 0, \tag{1}$$

where $T^{\mu\nu}$ is the energy-momentum tensor and N_i^μ are the net-charge four-currents.

These macroscopic fields can be decomposed with respect to the fluid flow velocity defined by Landau and Lifshitz [17], $u^\mu = T^{\mu\nu}u_\nu/e$, as

$$T^{\mu\nu} = eu^\mu u^\nu - P\Delta^{\mu\nu} + \pi^{\mu\nu}, \tag{2}$$

$$N_i^\mu = n_i u^\mu + V_i^\mu, \tag{3}$$

where $e = T^{\mu\nu}u_\mu u_\nu$ and $n_i = N_i^\mu u_\mu$ are the energy and net-charge densities in the local rest frame, respectively, $P = -T^{\mu\nu}\Delta_{\mu\nu}/3$ is the isotropic pressure, and $V_i^\mu = N_i^\alpha \Delta_\alpha^\mu$ are the charge diffusion currents. The shear-stress tensor, $\pi^{\mu\nu} = T^{\langle\mu\nu\rangle}$, is the traceless and orthogonal part of the energy-momentum tensor. With the $(+,-,-,-)$ convention for the metric tensor $g^{\mu\nu}$, the projection tensor is $\Delta^{\mu\nu} = g^{\mu\nu} - u^\mu u^\nu$. The angular brackets $\langle\rangle$ denote an operator leading to the symmetric, traceless, and orthogonal to the flow velocity part of a tensor: $T^{\langle\mu\nu\rangle} = [\frac{1}{2}(\Delta_\alpha^\mu\Delta_\beta^\nu + \Delta_\beta^\mu\Delta_\alpha^\nu) - \frac{1}{3}\Delta^{\mu\nu}\Delta_{\alpha\beta}]T^{\alpha\beta}$.

Landau's matching condition allows one to associate the rest-frame densities with their equilibrium values, $e = e_0(T,\{\mu_i\})$ and $n_i = n_{i,0}(T,\{\mu_j\})$. The difference between the isotropic and equilibrium pressures defines the so-called bulk viscosity, $\Pi = P - P_0$.

Equations (2) and (3) can be closed by providing an equation of state (EoS), together with the equations determining the evolution of dissipative quantities $\pi^{\mu\nu}$, Π, and V_i^μ. These quantities represent the dissipative forces in the system as well as deviations from the local thermal equilibrium. In the Navier-Stokes approximation they are linearly proportional to the gradients of velocity and temperature, with proportionality coefficients for shear viscosity $\eta_s(T,\{\mu_i\})$, bulk viscosity $\zeta(T,\{\mu_i\})$, and charge diffusion $\kappa_i(T,\{\mu_j\})$ quantifying the transport properties of the matter.

It is well known that the bulk viscosity coefficient of a relativistic gas is about three orders of magnitude smaller than its shear viscosity coefficient, and it vanishes in the ultrarelativistic limit [18]. However, it is still important for relativistic systems around phase transitions; therefore, even if the bulk viscosity is negligible in the QGP-phase, it may be large near and below the phase transition [19]. A large bulk viscosity at those stages may or may not have a significant effect on the observables [20–25]. Since disentangling the effects of shear and bulk on the observed spectra is difficult, and beyond the scope of this work, we adopt the approach of Ref. [21]. We assume that bulk viscosity is large only in the vicinity of the QCD phase transition but due to the critical slowing down its effect is so small that it can be safely ignored.

At midrapidity the matter formed in ultrarelativistic collisions at the RHIC and at the LHC is to a good approximation net-baryon free, and thus in boost-invariant calculations it has been an excellent approximation to neglect all conserved charges. Since in this study we want to investigate the backward and forward rapidity regions of the system where net-baryon density is finite, in principle we should include the net-baryon current and baryon charge diffusion in the description of the system. However, the baryon charge diffusion in a QGP as well as in a hadron gas is largely unknown at the moment. Also, at low values of net-baryon density where the lattice QCD results [26,27] can be used, the effect of the finite density on the EoS is small [28]. Therefore, to simplify the description of the system, and to allow us to concentrate solely on the effects of shear viscosity on the spectra, we ignore the finite baryon charge in the fluid as well. Thus we are left with the shear-stress tensor $\pi^{\mu\nu}$ as the only dissipative quantity in the system.

In so-called second-order or causal fluid-dynamical theories by Müller and by Israel and Stewart [29–31], the dissipative quantities fulfill certain coupled relaxation equations. Here we recall the relaxation equation for the shear-stress tensor obtained from the relativistic Boltzmann equation [32–34],

$$\begin{aligned}\tau_\pi D\pi^{\mu\nu} = {} & 2\eta_s\sigma^{\mu\nu} - \pi^{\mu\nu} - \tau_\pi(\pi^{\lambda\mu}u^\nu + \pi^{\lambda\nu}u^\mu)Du_\lambda \\ & - \delta_{\pi\pi}\pi^{\mu\nu}\theta - \tau_{\pi\pi}\pi_\lambda^{\langle\mu}\sigma^{\nu\rangle\lambda} \\ & + 2\tau_\pi\pi_\lambda^{\langle\mu}\omega^{\nu\rangle\lambda} + \varphi_7\pi_\lambda^{\langle\mu}\pi^{\nu\rangle\lambda}.\end{aligned} \tag{4}$$

Here τ_π is the shear-stress relaxation time, $D\pi^{\mu\nu} = u^\alpha\pi^{\mu\nu}_{;\alpha}$ denotes the time derivative, θ is the expansion rate, $\sigma^{\mu\nu}$ is the shear tensor, and $\omega^{\mu\nu}$ is the vorticity. The other coefficients can be calculated self-consistently from microscopic theory and, for example, in case of an ultrarelativistic massless Boltzmann gas we obtain, in the 14-moment approximation, $\tau_\pi = \frac{5}{3}\lambda_{mfp}$, $\delta_{\pi\pi} = (4/3)\,\tau_\pi$, $\tau_{\pi\pi} = (10/7)\,\tau_\pi$, while $\varphi_7 = (9/70)\,/P_0$, where λ_{mfp} is the mean free path between collisions. For QCD these coefficients are mostly unknown; however, for high-temperature QCD matter the coefficients given above may be acceptable as a first approximation.

For the sake of simplicity we ignore the last two terms in Eq. (4). This is justified since the relative contribution of the φ_7 coefficient was shown to be negligible compared to the others [34]. Similarly, we have observed that the term proportional to the vorticity has little effect on the overall evolution of the system and is thus omitted from the final calculations shown here.

B. The freeze-out stage

During the fluid-dynamical evolution the system cools and dilutes due to the expansion, and consequently the microscopic rescattering rate of particles, $\Gamma \sim n\sigma \simeq \lambda_{mfp}^{-1}$, decreases, until the rescatterings cease and particles stream freely toward detectors. The transition from an (almost) equilibrated fluid

to free-streaming particles is a gradual process, but since implementing such a gradual process into a fluid-dynamical description is very complicated [35,36], it is usually assumed to take place on an infinitesimally thin space-time layer, on the so-called freeze-out surface. Therefore the total number of particles crossing the surface Σ, with a normal vector $d^3\Sigma_\mu$ pointing outward, leads to the following invariant distribution of particles emitted from the fluid, known as the Cooper-Frye formula [37]:

$$E\frac{d^3N}{d^3p} = \int_\Sigma d^3\Sigma_\mu(x)\, p^\mu f(x,p), \tag{5}$$

where $p^\mu = (E,\mathbf{p})$ denotes the four-momentum, while $f(x,p)$ is the phase-space distribution function of particles on the surface.

To apply the Cooper-Frye formula, we need an appropriate criterion for choosing the surface Σ. Since scattering rates strongly depend on temperature, the usual approach is to assume the freeze-out to take place on a surface of constant temperature or energy density. However, it has been argued that it would be more physical to assume that the freeze-out happens when the average scattering rate is roughly equal to the expansion rate of the system [38].

This latter, so-called dynamical freeze-out, criterion can be expressed in terms of the Knudsen number, Kn, which is the ratio of a characteristic microscopic time or length scale, such as λ_{mfp}, and a characteristic macroscopic scale of the fluid, such as the inverse of the local gradients, $L^{-1} \approx \partial_\mu$. In terms of the Knudsen number the dynamical freeze-out criterion is Kn ≈ 1, which has occasionally been used in ideal fluid calculations [15,16,39,40], but for viscous fluids it is more appropriate to use the relaxation times of dissipative quantities as the microscopic scale, since they appear naturally in the evolution equations for dissipative quantities [32].

In most of our calculations we use the conventional constant-temperature freeze-out, but to evaluate how sensitive our results are to the particular freeze-out criterion, and to the freeze-out description in general, we also do the calculations assuming freeze-out at constant Knudsen number. We take the relaxation time of shear stress, τ_π, as the microscopic scale and the inverse of the expansion rate of the system, θ^{-1}, as the macroscopic scale. Thus we get a local Knudsen number of

$$\mathrm{Kn} = \tau_\pi \theta. \tag{6}$$

Since the Knudsen number can be evaluated in many different ways [14], we do not insist on freeze-out at Kn $= 1$, but we treat the freeze-out Knudsen number as a free parameter chosen to reproduce rapidity and p_T distributions of experimental data. To avoid pathologies encountered in Refs. [14,15], we also require that the dynamical freeze-out takes place below a temperature of $T = 180$ MeV and above $T = 80$ MeV.

To evaluate the distributions on the freeze-out surface, we assume that the distribution of particles for each species i, i.e., $f_i(x,p)$, is given by the well-known Grad's 14-moment ansatz, which includes corrections δf_i (shear viscosity only) to the local equilibrium distribution function as

$$f_i(x,p) \equiv f_{0i} + \delta f_i = f_{0i}\left[1 + (1 \mp \tilde{f}_{0i})\frac{p_i^\mu p_i^\nu \pi_{\mu\nu}}{2T^2(e+p)}\right], \tag{7}$$

where f_{0i} is the local equilibrium distribution function,

$$f_{0i}(x,p) = \frac{g_i}{(2\pi)^3}\left[\exp\left(\frac{p_i^\mu u_\mu - \mu_i}{T}\right) \pm 1\right]^{-1}, \tag{8}$$

and $\tilde{f}_{0i} = (2\pi)^3 f_{0i}/g_i$. We also include the contribution from all strong and electromagnetic two- and three-particle decays of the hadronic resonances up to a mass of 2 GeV to the final particle distributions.

The flow anisotropies are defined from a Fourier decomposition of the particle spectra as

$$E\frac{d^3N}{d^3p} = \frac{d^2N}{2\pi p_T dp_T dy_p}\left(1 + 2\sum_{n=1}^{\infty} v_n \cos n(\phi - \Psi_n)\right), \tag{9}$$

where $y_p = \frac{1}{2}\ln[(p^0 + p^z)/(p^0 - p^z)]$ is the rapidity of the particle, $p_T = \sqrt{p_x^2 + p_y^2}$ is its transverse momenta, and Ψ_n is the event plane for coefficient v_n. The Fourier coefficients $v_n = v_n(p_T, y_p)$ are the differential flow components. In this work the differential and integrated v_n are calculated by using the event-plane method.

III. PARAMETERS

We mostly implement the parametrization used in Refs. [11,13], but we retune the parameter values and generalize it for a (3+1)-dimensional non-boost-invariant case.

A. Equation of state

For the EoS we use the $s95p$-PCE-v1 parametrization of lattice QCD results at zero net-baryon density [41]. The high-temperature part of the EoS is given by the hotQCD Collaboration [42,43] and it is smoothly connected to the low-temperature part described as a hadron resonance gas, where resonances up to a mass of 2 GeV are included. The hadronic part includes a chemical freeze-out at $T_{\mathrm{chem}} = 150$ MeV where all stable particle ratios are fixed [44–46]. Since the construction of the EoS assumes that the entropy per particle is conserved after chemical freeze-out, the small (approximately 1%) entropy increase during the viscous hydrodynamical evolution below T_{chem} leads to a small increase in particle yields too.

B. Transport coefficients

As in our earlier works [11–13], we use four different parametrizations of the temperature-dependent shear viscosity over entropy ratio (see Fig. 1):

(1) LH-LQ, in which $(\eta_s/s)(T) = 0.08$ for all temperatures;
(2) LH-HQ, in which $(\eta_s/s)(T) = 0.08$ for the hadronic phase, while above T_{tr} the viscosity to entropy ratio

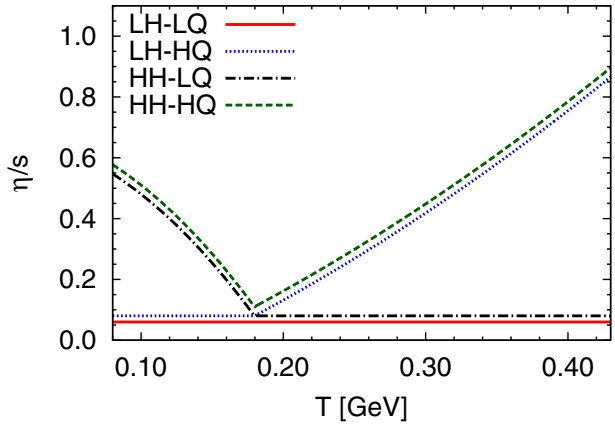

FIG. 1. (Color online) Different parametrizations of η_s/s as a function of temperature. The LH-LQ line has been shifted downward and the HH-HQ upward for better visibility.

increases according to

$$(\eta_s/s)(T)_{\rm QGP} = -0.289 + 0.288\,\frac{T}{T_{\rm tr}} + 0.0818\left(\frac{T}{T_{\rm tr}}\right)^2; \qquad (10)$$

(3) HH-LQ, in which, in the hadronic phase below $T_{\rm tr}$,

$$(\eta_s/s)(T)_{\rm HRG} = 0.681 - 0.0594\,\frac{T}{T_{\rm tr}} - 0.544\left(\frac{T}{T_{\rm tr}}\right)^2, \qquad (11)$$

while in the QGP-phase $(\eta_s/s)(T) = 0.08$; and

(4) HH-HQ, in which we use $(\eta_s/s)(T)_{\rm HRG}$ and $(\eta_s/s)(T)_{\rm QGP}$ for the hadronic and QGP phases, respectively.

Unless stated otherwise, the value of η_s/s at the transition temperature, $T_{\rm tr} = 180\,\text{MeV}$, is $(\eta_s/s)(T_{\rm tr}) = 0.08$. This is a close approximation to the lower bound conjectured in the framework of the AdS/CFT correspondence [5]. For all parametrizations the relaxation time for the shear-stress tensor is

$$\tau_\pi = 5\frac{\eta_s}{e+p}. \qquad (12)$$

For the sake of comparison, we also do the calculations using zero shear viscosity, i.e., for an ideal fluid.

C. The initial state

In this work we ignore the effects of event-by-event fluctuations [47,48], and we generalize a simple optical Glauber model [49] for a non-boost-invariant initial state. In different variants of the Glauber model the initial energy density in the transverse plane at midrapidity and at initial time τ_0 is given as a function of the density of binary collisions, $n_{\rm BC}(x,y,b)$, wounded nucleons, $n_{\rm WN}(x,y,b)$, or both:

$$e_T(\tau_0,x,y,b) = C_e(\tau_0)\, f(n_{\rm BC},n_{\rm WN}), \qquad (13)$$

where the normalization constant $C_e(\tau_0)$ is selected to reproduce the multiplicity measured in central collisions, and b is the impact parameter of the collision. In the following we use our BCfit parametrization [11,13], where the energy density depends solely on the number of binary collisions:

$$f_{\rm BC}(n_{\rm BC},n_{\rm WN}) = n_{\rm BC} + c_1 n_{\rm BC}^2 + c_2 n_{\rm BC}^3, \qquad (14)$$

and the coefficients c_1 and c_2 are chosen to reproduce the observed centrality dependence of multiplicity.

In the optical Glauber model, the density of binary collisions on the transverse plane is calculated from

$$n_{\rm BC}(x,y,b) = \sigma_{\rm NN} T_A(x+b/2,y)\, T_B(x-b/2,y), \qquad (15)$$

where $\sigma_{\rm NN}$ is the total nucleon-nucleon inelastic cross section, and $T_{A/B}$ is the nuclear thickness function. As a cross section we use $\sigma_{\rm NN} = 42$ mb at the RHIC [49,50] and $\sigma_{\rm NN} = 64$ mb at the LHC [51]. As usual, we define the thickness function as

$$T_A(x,y) = \int_{-\infty}^{\infty} dz\, \rho_A(x,y,z), \qquad (16)$$

where ρ_A is the Woods-Saxon nuclear density distribution,

$$\rho_A(\mathbf{r}) = \frac{\rho_0}{1+\exp[(r-R_A)/d]}, \qquad (17)$$

and $\rho_0 = 0.17$ fm^{-3} is the ground-state nuclear density and $d = 0.54$ fm is the surface thickness. The nuclear radii R_A are calculated from $R_A = 1.12A^{1/3} - 0.86/A^{1/3}$, which gives $R_{Au} \simeq 6.37$ fm and $R_{Pb} \simeq 6.49$ fm ($A_{Au} = 197$ and $A_{Pb} = 208$).

Unfortunately, there are very few theoretical constraints for the longitudinal structure of the initial state, since even the most sophisticated approaches to calculate the initial state from basic principles [52,53] are restricted to midrapidity. Here we follow the simple approaches shown in Refs. [54–56], and in a similar fashion we assume longitudinal scaling flow, $v_z = z/t$, i.e., $v_\eta = 0$, and a constant energy density distribution around midrapidity [57], followed by exponential tails in both backward and forward directions. We parametrize the longitudinal energy density distribution as

$$e_L(\eta) = \exp\left(-2c_\eta\sqrt{1+\frac{(|\eta|-\eta_0)^2}{2c_\eta\sigma_\eta^2}\Theta(|\eta|-\eta_0)} + 2c_\eta\right), \qquad (18)$$

where $\eta = \frac{1}{2}\ln[(t+z)/(t-z)]$ is the space-time rapidity, and $\Theta(x)$ is the Heaviside step function. Thus the normalized energy density distribution is

$$e(\tau_0,x,y,\eta,b) = e_T(\tau_0,x,y,b)\, e_L(\eta). \qquad (19)$$

We are aware that there are more sophisticated approaches in the literature [22,58–60], but since attempts to create more plausible longitudinal structures easily lead to a rapidity distribution of v_2 which strongly deviates from the observed one [54], we leave the detailed study of the longitudinal structures for a later work.

Due to entropy production in dissipative fluids, the different parametrizations of η_s/s lead to different entropy production and therefore different final multiplicity of hadrons. Because

most of the entropy is produced during the early stages of the expansion when the longitudinal gradients are largest [61], it is sufficient to adjust initial densities according to the entropy produced in the partonic phase. Further entropy production during the hadronic evolution turns out to represent only a small contribution in the final multiplicities and it is not corrected in our calculations.

At the RHIC, we used the following maximum energy densities, $e_0 = e(\tau_0,0,0,0)$:

(i) for an ideal fluid, $e_0 = 17.0$ GeV/fm^3,
(ii) for LH-LQ and HH-LQ, $e_0 = 15.8$ GeV/fm^3, and
(iii) for LH-HQ and HH-HQ, $e_0 = 14.9$ GeV/fm^3,

while at the LHC

(iv) for an ideal fluid, $e_0 = 57.5$ GeV/fm^3,
(v) for LH-LQ and HH-LQ, $e_0 = 54.5$ GeV/fm^3, and
(vi) for LH-HQ and HH-HQ, $e_0 = 49.5$ GeV/fm^3.

Note that these values are smaller than the ones given in Refs. [11,13]. The main reason for this is that we used different data to fit the centrality dependence, and we chose to fit the multiplicity as a function of centrality class, not as a function of number of participants, as was done in Refs. [11,13]. This leads to different values of c_1 and c_2 parameters, and, consequently, the maximum density in a head-on collision (which practically never happens) is different even if the energy density at midrapidity at impact parameters $b > 2$ fm is almost identical.

The parameters controlling the centrality dependence, c_1 and c_2 in Eq. (14), are $c_1 = -0.035$ fm^{-2} and $c_2 = 0.00034$ fm^{-4} at the RHIC and $c_1 = -0.02$ fm^{-2} and $c_2 = 0.000175$ fm^{-4} at the LHC. The parameters in Eq. (18) defining the longitudinal structure are $c_\eta = 4$ at the RHIC and $c_\eta = 2$ at the LHC, while $\eta_0 = 2.0$ for the constant-rapidity plateau for both. The width of the rapidity distribution is $\sigma_\eta = 1.0$ at the RHIC and $\sigma_\eta = 1.8$ at the LHC. The average impact parameters in each centrality class are given in Table I.

If not stated otherwise the fluid-dynamical evolution is started at $\tau_0 = 1$ fm/c proper time. The initial values for the transverse fluid velocity and shear-stress tensor are always set to zero. The value of the decoupling temperature or Knudsen number is indicated in the figures.

To obtain the final particle distributions we use the framework described in Ref. [62]. Thus we sample particle distributions to create "events" even if we are not doing event-by-event calculations, but we use conventional averaged initial states. The particle spectra and other measurables at the RHIC are obtained as an average over $N_{ev} = 100\,000$ events, where the sampling is done over $p_T = (0,5.4)$ GeV and $\eta_{\rm ch} = (-6.6,6.6)$ with $N_{p_T} = 36$ and $N_{\eta_{\rm ch}} = 22$ bins. At the LHC the particle multiplicity is $\simeq 2.5$ times larger than at the RHIC; hence we average over $N_{ev} = 40\,000$ events.

TABLE I. The average impact parameter b in each centrality class at the RHIC and the LHC.

Centrality (%)	RHIC b (fm)	LHC b (fm)
0–5	2.24	2.32
5–10	4.09	4.24
10–20	5.78	5.99
20–30	7.49	7.76
30–40	8.87	9.19
40–50	10.06	10.43

IV. RESULTS AND COMPARISONS TO DATA

A. Au + Au at $\sqrt{s_{\rm NN}} = 200$ GeV at the RHIC

We fix the parameters characterizing the initial state, Eqs. (13), (14), and (18), by comparison to the PHOBOS charged particle pseudorapidity distribution, $dN_{\rm ch}/d\eta_{\rm ch}$, at various centralities [63]. We present our results in Fig. 2, where the calculations are shown for 0%–5% centrality and for the average of 10%–20% and 20%–30% as well as 30%–40% and 40%–50% centralities. This is in order to facilitate a comparison to the data taken at 0%–6%, 15%–25%, and 35%–45% centralities. As required, the final multiplicity and pseudorapidity distribution are well reproduced at all centralities for all parametrizations of the temperature-dependent shear viscosity to entropy density ratio. Here we once again stress the importance of fixing the initial energy density to compensate for the entropy production for different η_s/s parametrizations. Otherwise, for fixed initial densities, the larger the effective viscosity, the larger the entropy production and thus the final multiplicity.

The kinetic freeze-out temperature, $T_{\rm dec}$, affects the charged particle pseudorapidity distribution very weakly. We have chosen $T_{\rm dec} = 100$ MeV by comparison to the pion, kaon, and proton p_T spectra measured by the PHENIX Collaboration [64], and we checked that, if we use $T_{\rm dec} = 140$ MeV, the pseudorapidity distributions are still within error bars and

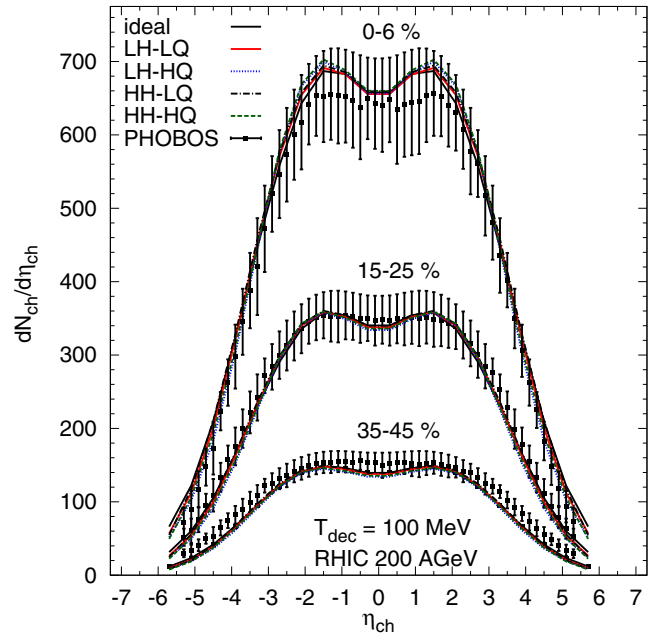

FIG. 2. (Color online) The charged particle pseudorapidity distribution $dN_{\rm ch}/d\eta_{\rm ch}$. Experimental data are from the PHOBOS Collaboration [63].

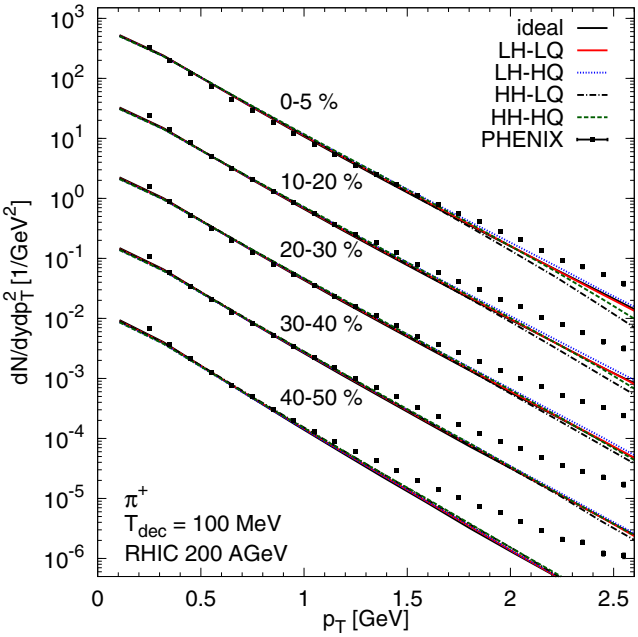

FIG. 3. (Color online) Transverse momentum spectra of positive pions at the RHIC. Experimental data are from the PHENIX Collaboration [64].

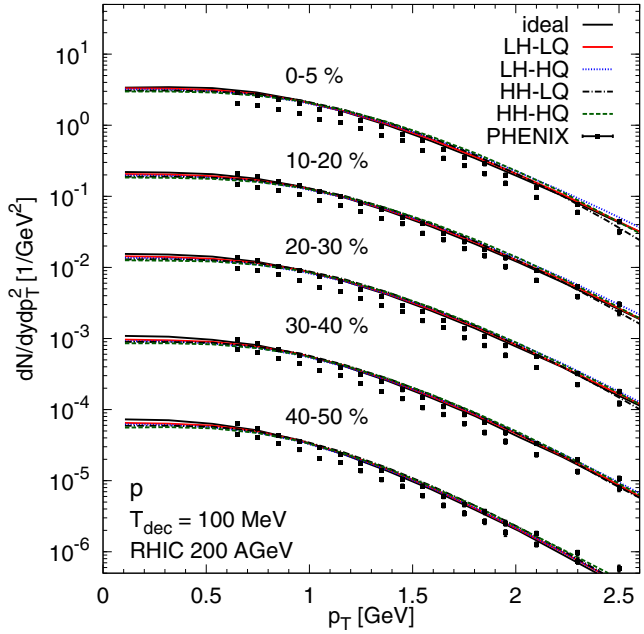

FIG. 5. (Color online) Transverse momentum spectra of protons at the RHIC. Experimental data for protons (upper) and antiprotons (lower) are from the PHENIX Collaboration [64].

that the change is on the same level as the differences due to different viscosities shown in Fig. 2. Such a weak dependence is not surprising: It is well known that, in a chemically frozen system, pion p_T distributions are weakly sensitive to the kinetic freeze-out temperature [65]. We now observe similar behavior in the longitudinal direction.

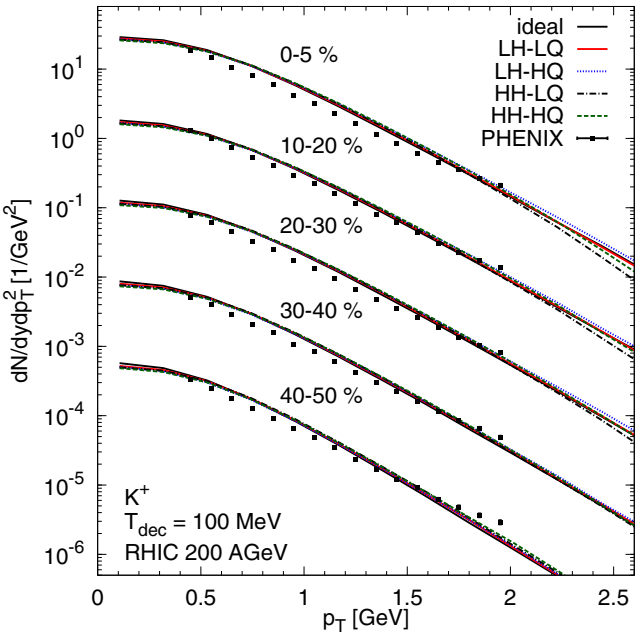

FIG. 4. (Color online) Transverse momentum spectra of positive kaons at the RHIC. Experimental data are from the PHENIX Collaboration [64].

In Figs. 3, 4, and 5 we present the p_T spectra of positive pions, kaons, and protons, respectively, corresponding to centrality classes, 0%–5%, 10%–20%($\times 10^{-1}$), 20%–30%($\times 10^{-2}$), 30%–40%($\times 10^{-3}$), and 40%–50%($\times 10^{-4}$). Here the multiplicative factors are applied (to both theoretical and experimental points) for better visibility. The experimental data are from the PHENIX Collaboration [64].

As seen before in viscous calculations (e.g., in Ref. [13]), the slopes of pion spectra are reasonably well reproduced up to $p_T \simeq 1.5$ GeV for semicentral collisions, but the agreement recedes with increasing impact parameter. The kaon yields are overpredicted at all centralities, whereas the fit to proton spectra is slightly better than the fit to kaons. Since we do not include a finite baryochemical potential in our calculation, we are consistently overestimating the yields of heavy particles, which might imply the need for even lower chemical freeze-out temperature.

The pion spectra become flatter with increasing freeze-out temperature; hence, for example, for $T_{\rm dec} = 140$ MeV the theoretical calculations are in a better agreement at larger momenta, but then we overestimate the spectra around $p_T \sim 1$ GeV. The slope of the proton spectra become steeper with increasing freeze-out temperature as well, and thus $T_{\rm dec} = 100$ MeV provides the best compromise.

As expected, after the initial densities are fixed to reproduce the yield, the slopes are practically unaffected by the different η_s/s parametrizations, and the corresponding δf_i in each case represents only a small correction compared to the thermal spectra.

In Figs. 6 and 7 the elliptic flow coefficient v_2 at various centralities is shown as a function of transverse momentum p_T and pseudorapidity $\eta_{\rm ch}$. In Fig. 6 the experimental data are from the STAR Collaboration [66], whereas in Fig. 7

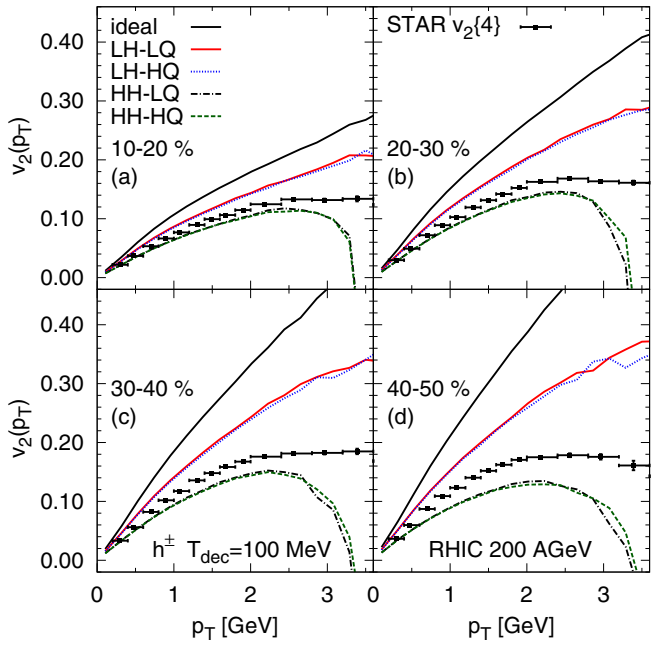

FIG. 6. (Color online) Charged hadron $v_2(p_T)$ at the RHIC. Experimental data are from the STAR Collaboration [66].

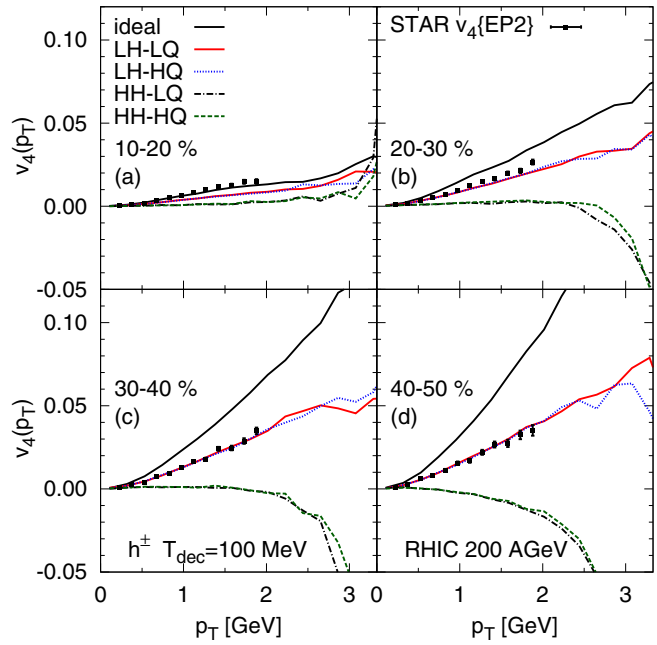

FIG. 8. (Color online) Charged hadron $v_4(p_T)$ at the RHIC. Experimental data are from the STAR Collaboration [68].

the average of 0%–5% and 10%–20% and of 10%–20% and 20%–30% events are compared to the data from the PHOBOS Collaboration for 3%–15% and 15%–25% centrality classes [67] and to the STAR Collaboration data in the 15%–25% centrality class [68].

As expected, the p_T differential elliptic flow coefficient shows the behavior reported in Refs. [11,13]: At the RHIC the elliptic flow coefficient is very sensitive to viscosity in the hadronic phase but independent of the high-temperature parametrization of the viscosity. The same observation also holds for the rapidity-dependent elliptic flow coefficient at all centrality classes. The dissipative reduction of v_2 is quite independent of rapidity, and thus we cannot reproduce the shape of $v_2(\eta_{\rm ch})$ very well. On the other hand, slightly larger hadronic viscosity would further reduce v_2, and our result would be very close to the ideal fluid + UrQMD hybrid calculation of Ref. [69].

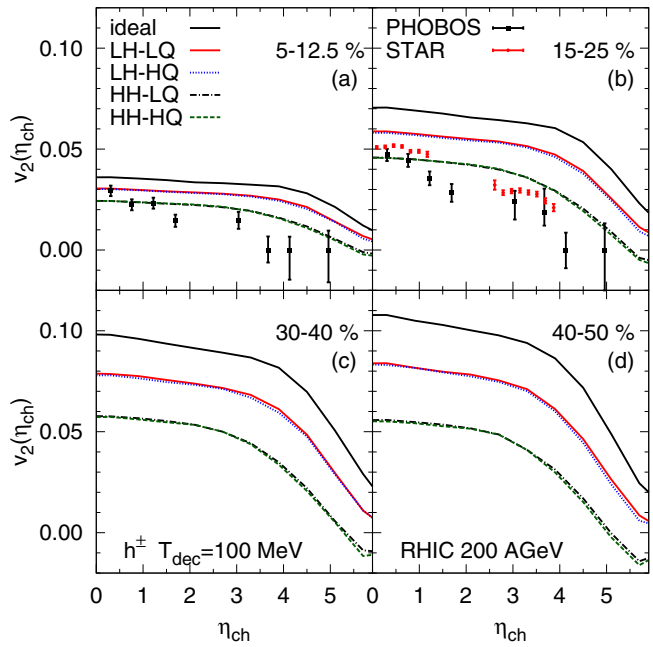

FIG. 7. (Color online) Charged hadron $v_2(\eta_{\rm ch})$ at the RHIC. Experimental data are from the PHOBOS [67] and STAR [68] Collaborations.

Similarly, the $v_4(p_T)$ and $v_4(\eta_{\rm ch})$ of charged hadrons in different centrality classes are compared to the experimental data from the STAR Collaboration [68] in Figs. 8 and 9. The v_4 coefficient, both as a function of transverse momentum and as a function of pseudorapidity, complies with the previously made observations about the elliptic flow coefficient. As we have reported earlier [12,13], v_4 is sensitive to viscosity at even later stages of the evolution than v_2, and a large hadronic viscosity is sufficient to turn $v_4(p_T)$ negative at quite low p_T. The comparison of Figs. 7 and 9 also shows the well-known fact that the larger the value of n, the stronger the viscous suppression of v_n [70,71]. Viscosity has only a weak effect on the shapes of $v_2(\eta_{\rm ch})$ and $v_4(\eta_{\rm ch})$, but quite interestingly the effect on the shapes is different for different coefficients: Increasing viscosity makes the (approximate) plateau in $v_2(\eta_{\rm ch})$ narrower but that in $v_4(\eta_{\rm ch})$ wider.

From Fig. 8 it is apparent that the $v_4(p_T)$ data favor the parametrizations with low hadronic viscosity, unlike $v_2(p_T)$. However, we have to remember that the experimental data were obtained by using different methods for v_2 and v_4, i.e., four-particle cumulant and mixed harmonic event-plane methods, whereas we use the event-plane method to evaluate all the harmonics. Another uncertainty is that event-by-event fluctuations cause a sizable fraction of v_4, but they are not included in our study. Thus we advise against drawing any

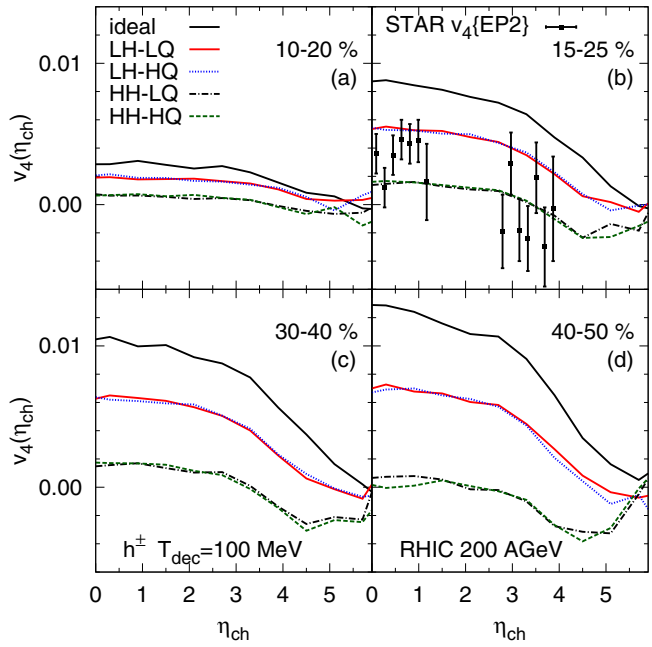

FIG. 9. (Color online) Charged hadron $v_4(\eta_{ch})$ at the RHIC. Experimental data are from the STAR Collaboration [68].

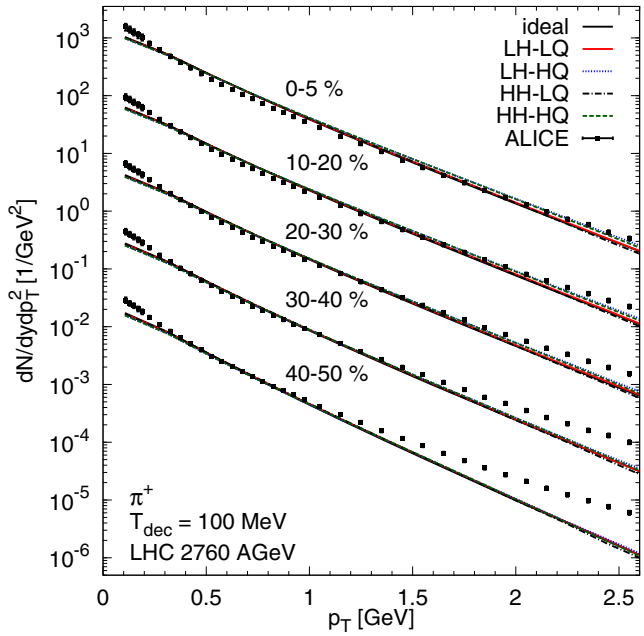

FIG. 11. (Color online) Transverse momentum spectra of positive pions at the LHC. Experimental data are from the ALICE Collaboration [73].

conclusions about the favored $(\eta_s/s)(T)$ from this particular result.

B. Pb + Pb at $\sqrt{s_{NN}} = 2760$ GeV at the LHC

As at the RHIC, we use the pseudorapidity distribution of charged particles to fix the initialization and the p_T distributions of identified particles to fix the kinetic freeze-out temperature.

In Fig. 10 the charged particle pseudorapidity distributions $dN_{ch}/d\eta_{ch}$ for different centrality bins are compared to the experimental data from the ALICE Collaboration [72]. The pseudorapidity distribution of charged particles reasonably matches the data for all centrality classes given in the figure. Similarly as for the RHIC we slightly overshoot the

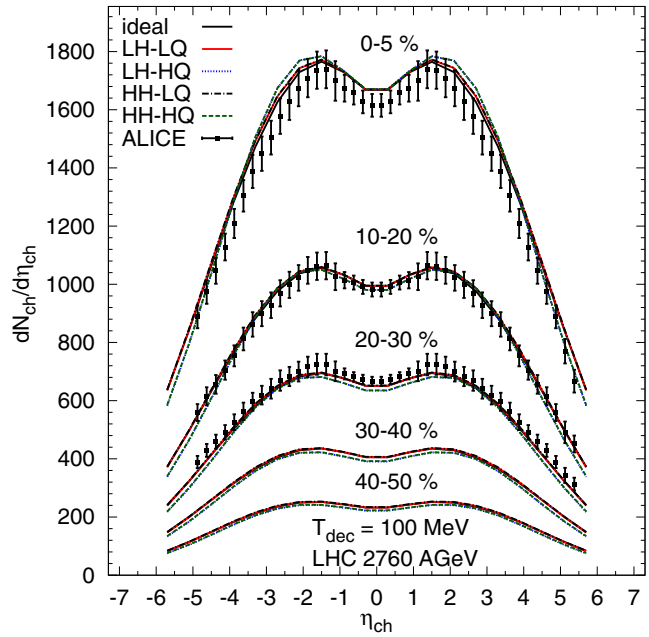

FIG. 10. (Color online) The charged particle pseudorapidity distribution $dN_{ch}/d\eta_{ch}$ at the LHC. Experimental data are from the ALICE Collaboration [72].

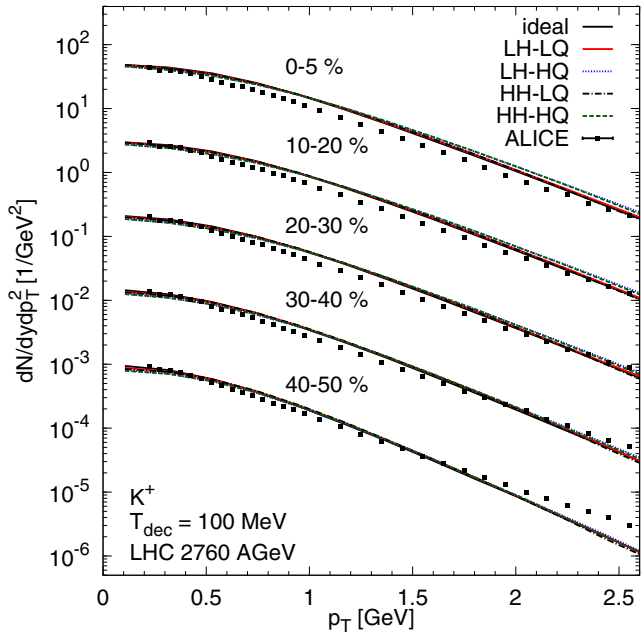

FIG. 12. (Color online) Transverse momentum spectra of positive kaons at the LHC. Experimental data are from the ALICE Collaboration [73].

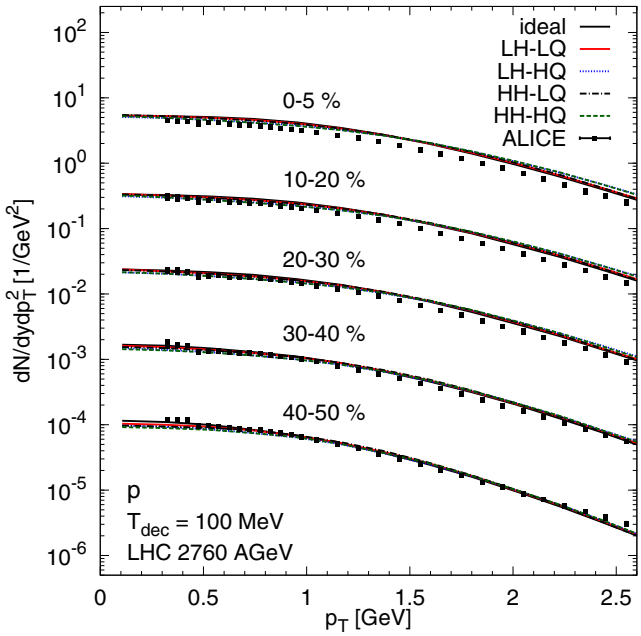

FIG. 13. (Color online) Transverse momentum spectra of protons at ALICE. Experimental data for protons and antiprotons are from the ALICE Collaboration [73].

experimental results at the LHC for the most central collisions while we undershoot for the peripheral ones. Moreover, as observed before, the pseudorapidity distributions of charged particles are insensitive to the chosen freeze-out temperature.

In Figs. 11, 12, and 13 we show the p_T spectra of positive pions, positive kaons, and protons corresponding to centrality classes, with multiplicative factors applied for

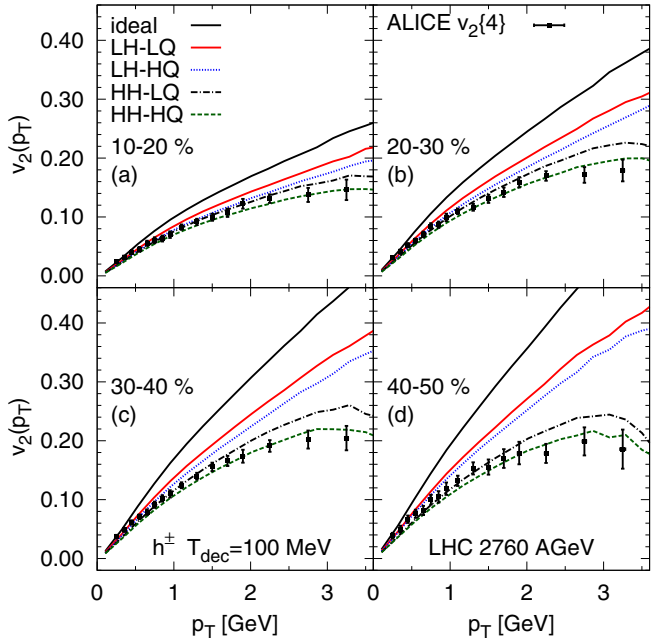

FIG. 14. (Color online) Charged hadron $v_2(p_T)$ at the LHC. Experimental data are from the ALICE Collaboration [75].

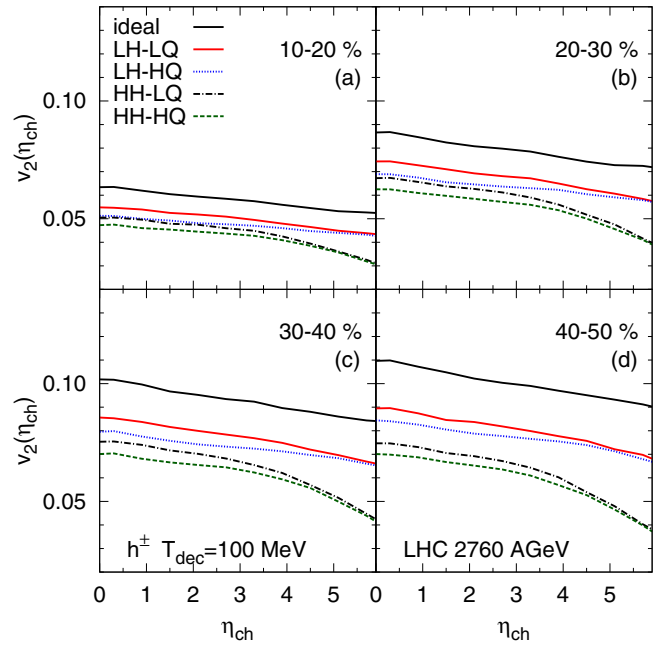

FIG. 15. (Color online) Charged hadron $v_2(\eta_{ch})$ at the LHC.

better visibility. The experimental data are from the ALICE Collaboration [73]. These distributions behave in a way similar to that of the RHIC results, and they are thus unaffected by the different η_s/s parametrizations. We note that, as in many other calculations [73,74], the low-p_T part of the pion distribution turned out to be very difficult to reproduce.

In Figs. 14 and 15 the elliptic flow coefficient v_2 is shown as functions of transverse momentum and pseudorapidity, respectively. In both figures the experimental data are from the ALICE Collaboration [75]. At the LHC viscous suppression

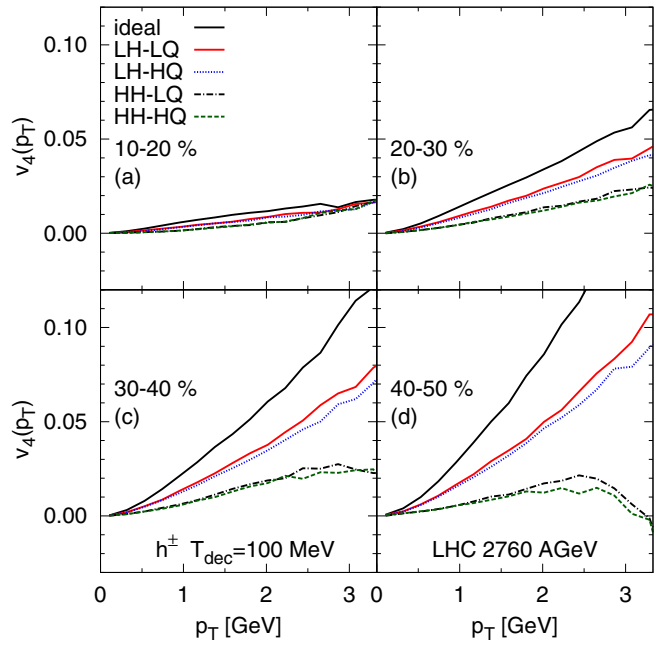

FIG. 16. (Color online) Charged hadron $v_4(p_T)$ at the LHC.

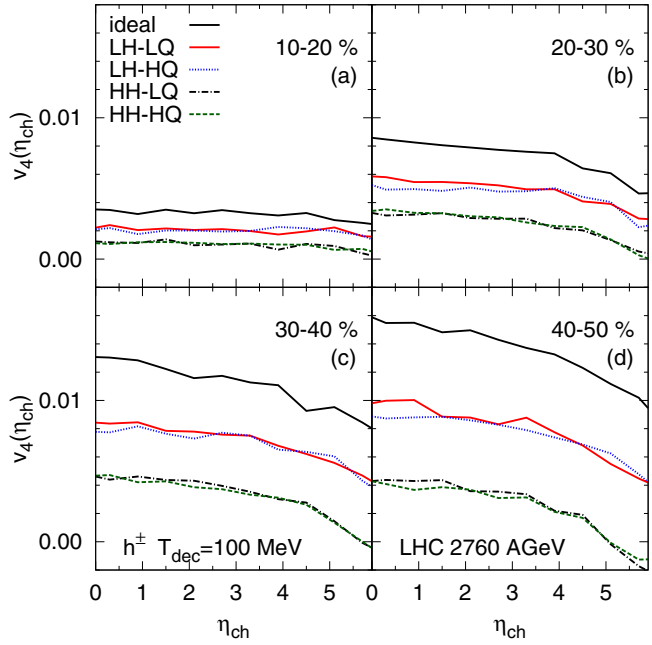

FIG. 17. (Color online) Charged hadron $v_4(\eta_{\rm ch})$ at the LHC.

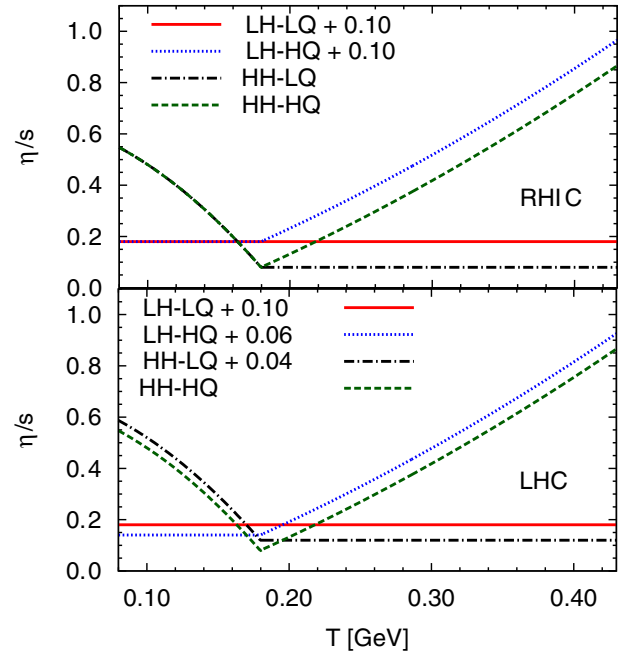

FIG. 18. (Color online) Parametrizations of $(\eta_s/s)(T)$ rescaled to lead to similar charged hadron $v_2(p_T)$ in central collisions at the RHIC (top) and the LHC (bottom).

of the elliptic flow is less dominated by the hadronic viscosity than at the RHIC. In central collisions at midrapidity, both QGP and hadronic viscosities affect v_2 equally: Large QGP viscosity may be compensated with a low hadronic viscosity and vice versa (compare LH-HQ with HH-LQ for 10%–20% and 20%–30% up to $p_T \leqslant 2$ GeV or $\eta_{\rm ch} \leqslant 2$). In peripheral collisions and at large rapidities, v_2 loses its sensitivity to QGP viscosity, and the system behaves like at the RHIC. Thus measuring v_2 at large rapidities at the LHC would provide an additional handle on the temperature dependence of the η_s/s ratio.

Finally, in Figs. 16 and 17 we present the v_4 coefficients as functions of p_T and $\eta_{\rm ch}$. As discussed in Refs. [12,13], v_4 is sensitive to viscosity at lower temperatures than is v_2. Therefore the behavior of v_4 at the LHC is similar to the behavior of v_4 and v_2 at the RHIC: The curves are grouped according to their hadronic viscosity, and they show no sensitivity to QGP viscosity. The suppression of v_4 at both the LHC and the RHIC is clearly sensitive to the hadronic viscosity (compare Fig. 8 with Fig. 16 and Fig. 9 with 17) and to the minimum value of η_s/s.

V. THE DISTINGUISHABILITY OF THE η_s/s PARAMETRIZATIONS

In the previous section we described how the sensitivity of v_2 and v_4 to QGP and hadronic shear viscosities depends on centrality, transverse momentum p_T, and pseudorapidity $\eta_{\rm ch}$. Now we use this observation to distinguish between different parametrizations of $(\eta_s/s)(T)$. We rescale our existing parametrizations in such a way that they all lead to almost identical p_T differential v_2 in central collisions, and we check whether the calculated v_2 and v_4 differ at other centralities and rapidities. Note that this procedure also tests the sensitivity of the flow coefficients to the minimum value of η_s/s and not only to its values above and below the transition temperature.

The new scaled parametrizations are shown in Fig. 18. At RHIC energies the value of the viscosity to entropy ratio for LH-LQ and LH-HQ is increased uniformly with $\Delta\eta_s/s = 0.1$ for all temperatures, while the other two parametrizations remain unchanged. Since the sensitivity to the temperature dependence of η_s/s is more complicated at the LHC, the required changes in parametrizations are $\Delta\eta_s/s = 0.1$ for LH-LQ, $\Delta\eta_s/s = 0.06$ for LH-HQ, and $\Delta\eta_s/s = 0.04$ for HH-LQ. The increase in η_s/s leads to larger entropy production, and thus to larger final multiplicities, which we have counteracted by rescaling the initial densities accordingly.

Note that since the LH-HQ and HH-LQ parametrizations require different rescalings at the RHIC and the LHC, they can be distinguished already by comparing $v_2(p_T)$ in central collisions at different energies, but LH-LQ and HH-HQ cannot. Furthermore, we want to check whether it is possible to distinguish LH-HQ and HH-LQ in collisions at the same energy by varying the centrality and rapidity.

In Figs. 19, 20, and 21 we present $v_2(p_T)$, $v_2(\eta_{\rm ch})$, and $v_4(p_T)$ at the RHIC using these new parametrizations. As required, in central collisions all parametrizations lead to similar $v_2(p_T)$—the differences due to different hadronic viscosity at very late stages of the evolution are compensated by the larger viscosity at and after the QCD transition region. However, when one moves to larger centralities, and thus to smaller systems, the region where v_2 is most sensitive to shear viscosity moves toward lower temperatures, and the parametrizations with different hadronic viscosities can be identified (see Fig. 19). The same, although weaker, phenomenon happens when we move to larger rapidities (see

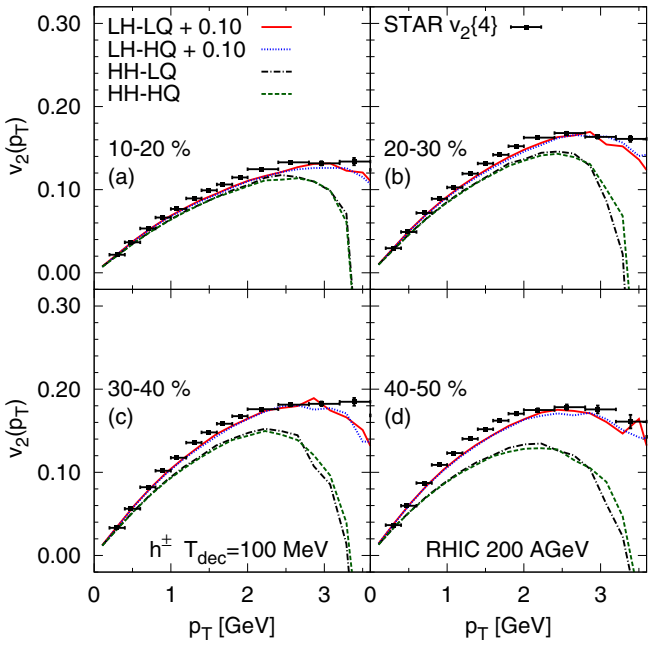

FIG. 19. (Color online) Charged hadron $v_2(p_T)$ at the RHIC. Experimental data are from the STAR Collaboration [66].

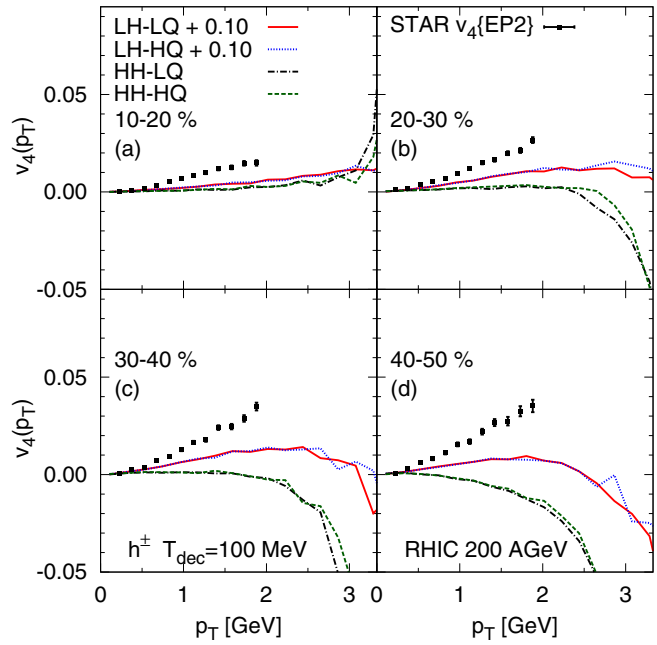

FIG. 21. (Color online) Charged hadron $v_4(p_T)$ at the RHIC. Experimental data are from the STAR Collaboration [68].

Fig. 20). Most of the sensitivity comes from the change in centrality, but, as seen in the 15%–25% centrality class [Fig. 20(b)], the difference at large rapidities increases faster than at midrapidity. On the other hand, the v_4 coefficient shows larger sensitivity than v_2: In central collisions all parametrizations are equal, but the difference increases with increasing fraction of cross section faster than for v_2. Note that none of the observables are sensitive to the plasma viscosity, but we have to study the collisions at the LHC to be able to distinguish, say, HH-LQ and HH-HQ parametrizations.

At the LHC we see slightly different behavior. In central collisions $v_2(p_T)$ is again the same for all parametrizations by construction, but the differences appear slowly and stay modest when we move toward more peripheral collisions (see Fig. 22). Again, in more peripheral collisions, the system is most sensitive to viscosity in lower temperatures, and $v_2(p_T)$ curves are

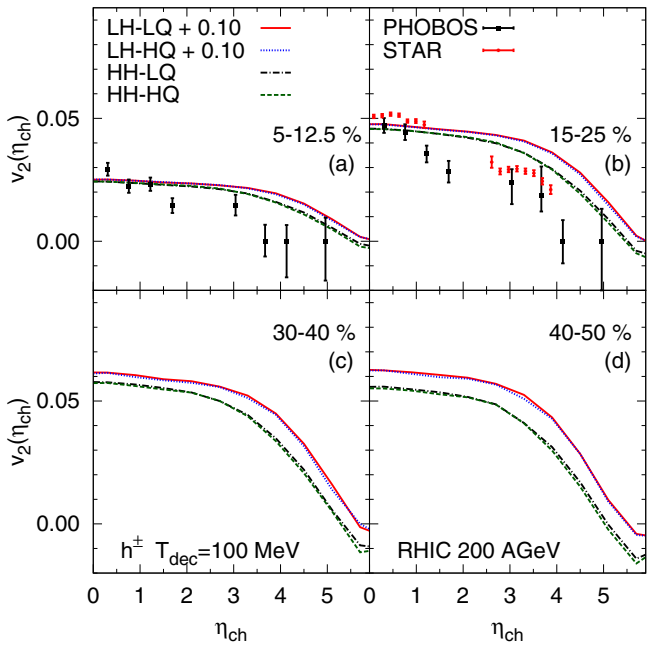

FIG. 20. (Color online) Charged hadron $v_2(\eta_{ch})$ at the RHIC. Experimental data are from the PHOBOS [67] and STAR [68] Collaborations.

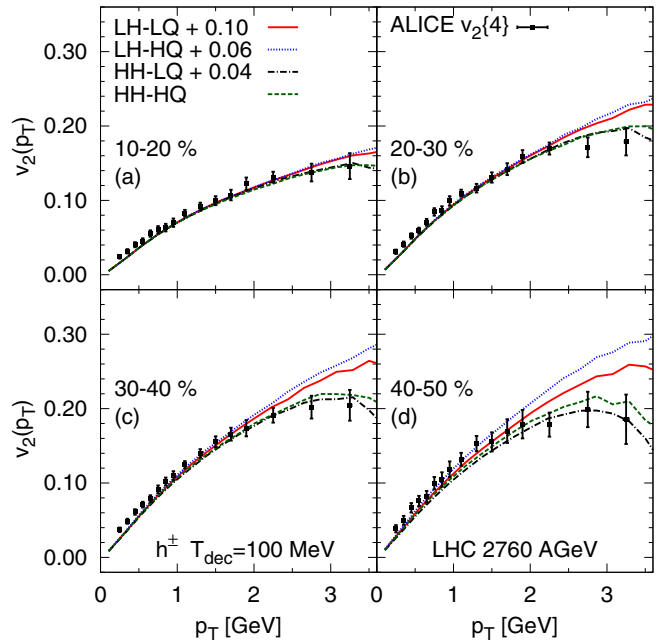

FIG. 22. (Color online) Charged hadron $v_2(p_T)$ at the LHC. Experimental data are from the ALICE Collaboration [75].

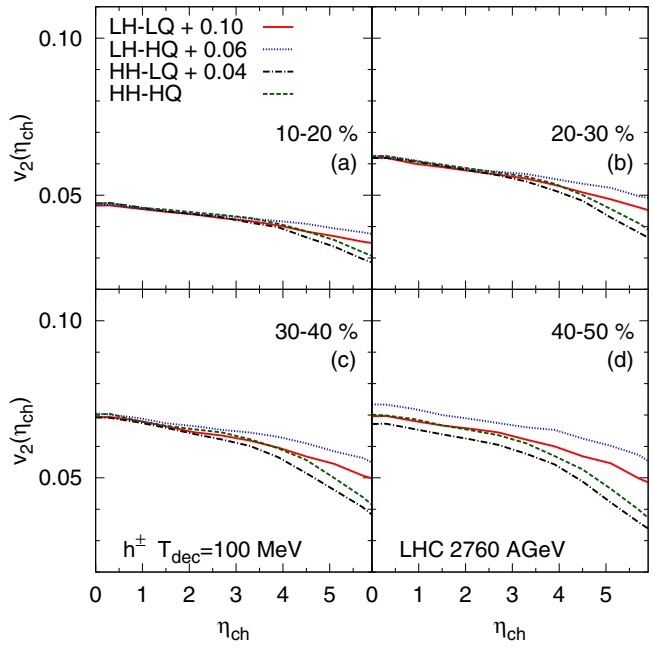

FIG. 23. (Color online) Charged hadron $v_2(\eta_{\rm ch})$ at the LHC.

ordered according to hadronic viscosity—the larger viscosity is at freeze-out, the lower is $v_2(p_T)$. In Fig. 15 the pseudorapidity distribution of v_2 showed clear sensitivity to shear viscosity. In that figure different parametrizations caused different v_2 already at midrapidity in central collisions. Now viscosity is scaled to remove this difference, and the sensitivity of the shape of $v_2(\eta_{\rm ch})$ to the viscosity is more visible. As one can see from Fig. 23, larger hadronic viscosity causes $v_2(\eta_{\rm ch})$ to drop slightly faster with increasing rapidity. The strongest difference is seen in $v_4(p_T)$, which is able to distinguish the new parametrizations at the LHC (see Fig. 24), but its resolving power at the LHC is weaker than at the RHIC (Fig. 21). Thus we conclude that differential measurements of the flow anisotropies as function of transverse momentum, pseudorapidity, and centrality can provide constraints for the temperature dependence of η_s/s, but the measurements at various energies are essential to constrain the parametrizations properly.

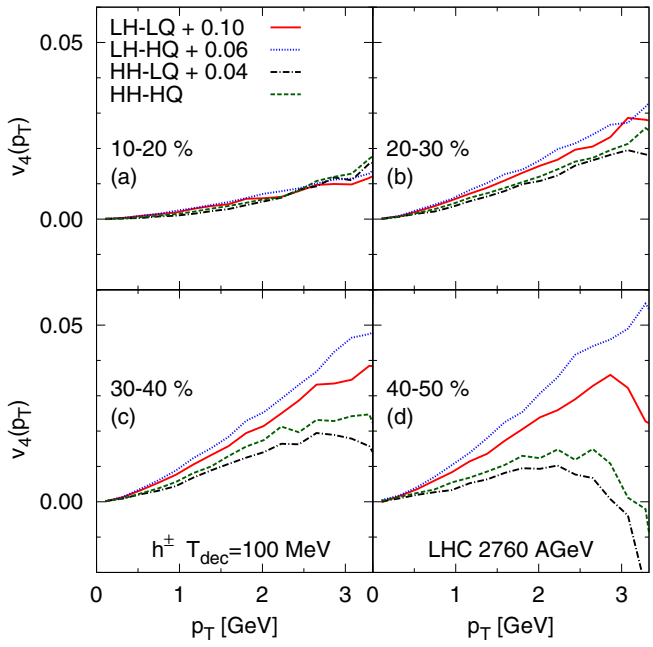

FIG. 24. (Color online) Charged hadron $v_4(p_T)$ at the LHC.

VI. DYNAMICAL FREEZE-OUT

To test the sensitivity of our results to the freeze-out criterion and the freeze-out description in general, we redo some of the calculations using the dynamical freeze-out criterion [38]. In these calculations we use only our HH-LQ and HH-HQ parametrizations for the shear viscosity, since the low value of η_s/s in a hadron gas leads to a very slowly increasing relaxation time and thus to unrealistically low temperatures, $\langle T\rangle \ll 80$ MeV, on the freeze-out surface when $\mathrm{Kn}_{\rm dec} \sim 1$. Since the Knudsen number can be based on many quantities [14], and since we do not know when exactly the hydrodynamical description should break down, we use the freeze-out Knudsen number as a free parameter chosen to fit the rapidity and p_T distributions.

Figures 25 and 26 show the charged particle pseudorapidity distributions at the RHIC and the LHC, respectively. As expected, the pseudorapidity distributions are only weakly dependent on the precise value of $\mathrm{Kn}_{\rm dec}$, but it turned out that our choice of Knudsen number and relaxation time lead to weak sensitivity of the p_T distributions to the value of $\mathrm{Kn}_{\rm dec}$ too. Nevertheless, we found that decoupling at constant Knudsen number $\mathrm{Kn}_{\rm dec} = 0.8$ leads to basically the same rapidity and p_T distributions as conventional decoupling at $T_{\rm dec} = 100$ MeV.

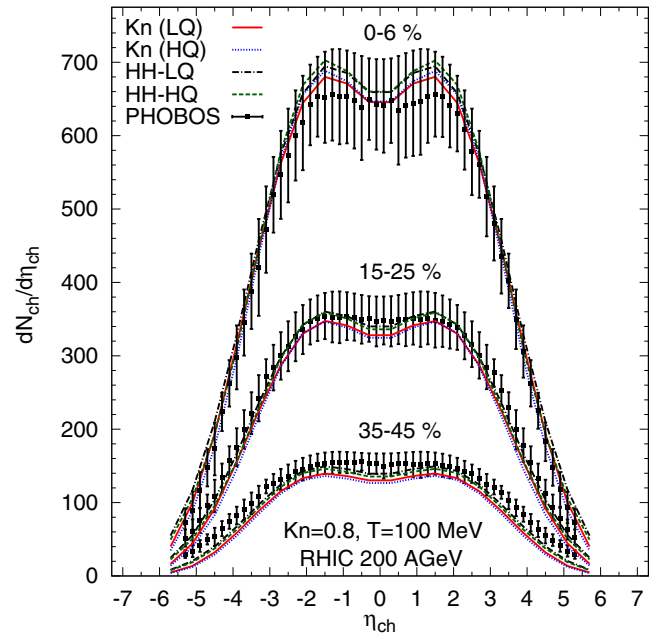

FIG. 25. (Color online) The charged particle pseudorapidity distribution $dN_{\rm ch}/d\eta_{\rm ch}$ at the RHIC obtained by using two different freeze-out criteria. Experimental data are from the PHOBOS Collaboration [63].

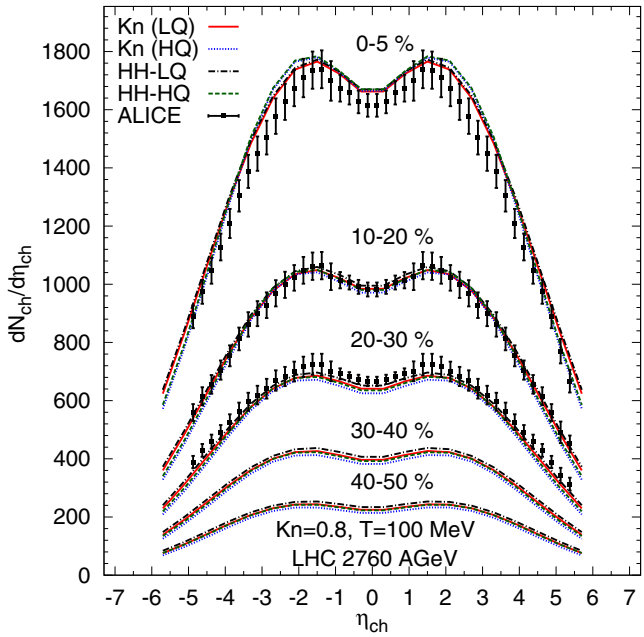

FIG. 26. (Color online) The charged particle pseudorapidity distribution $dN_{\rm ch}/d\eta_{\rm ch}$ at the LHC obtained by using two different freeze-out criteria. Experimental data are from the ALICE Collaboration [72].

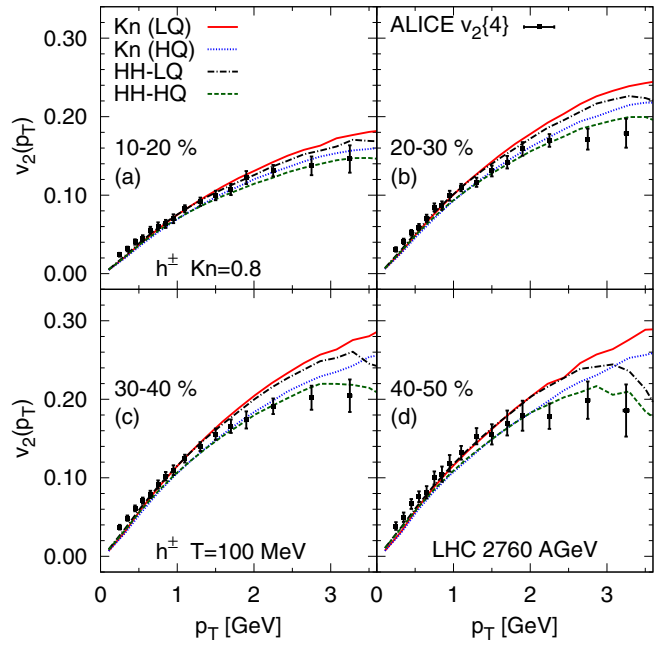

FIG. 28. (Color online) Charged hadron $v_2(p_T)$ at the LHC obtained by using two different freeze-out criteria. Experimental data are from the ALICE Collaboration [75].

The p_T differential v_2 of charged hadrons at the RHIC and the LHC is shown in Figs. 27 and 28, respectively. Unlike in Ref. [16], where both p_T distributions and anisotropies depended on the freeze-out criterion, we see that, once the freeze-out parameters are fixed to produce similar p_T distributions, the anisotropies become very similar. This is especially clear at the LHC. Below $p_T \sim 2$ GeV both criteria lead to identical $v_2(p_T)$, and the difference seen in the plots is due to the shear viscosity parametrization. At the RHIC both parametrizations lead to identical $v_2(p_T)$, and a weak sensitivity to the freeze-out criterion appears around $p_T \sim 1$ GeV. However, this sensitivity is too weak to be significant.

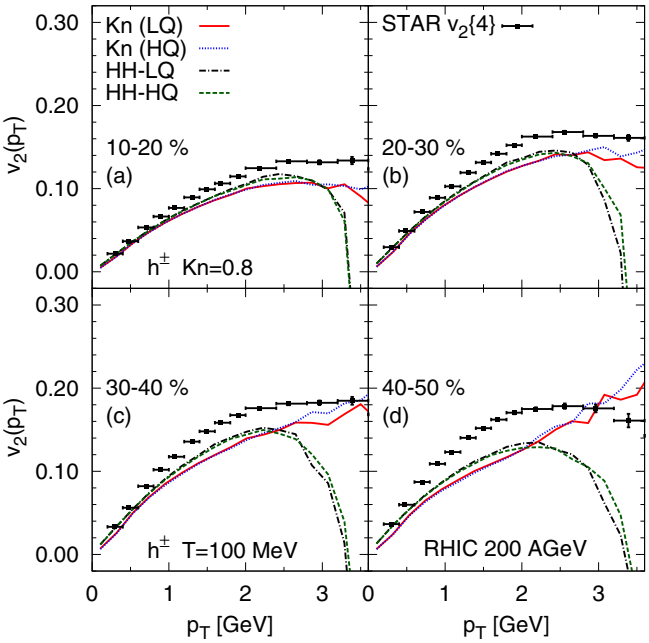

FIG. 27. (Color online) Charged hadron $v_2(p_T)$ at the RHIC obtained by using two different freeze-out criteria. Experimental data are from the STAR Collaboration [66].

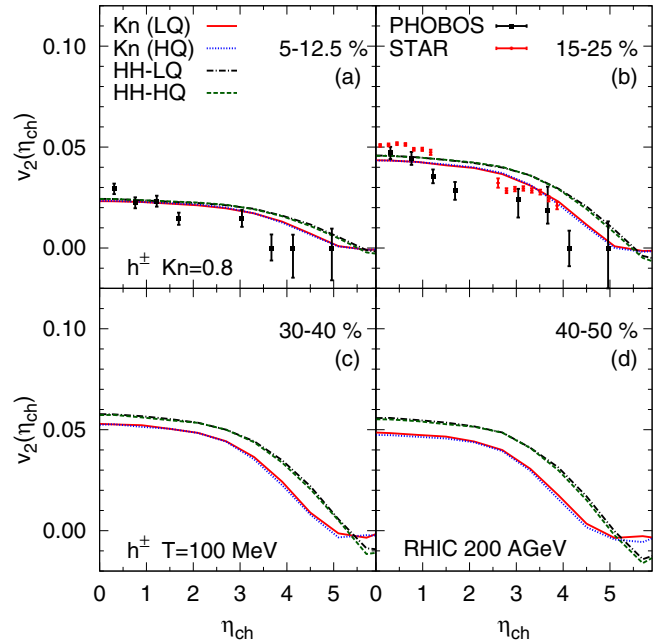

FIG. 29. (Color online) Charged hadron $v_2(\eta_{\rm ch})$ at the RHIC obtained by using two different freeze-out criteria. Experimental data are from the STAR Collaboration [66].

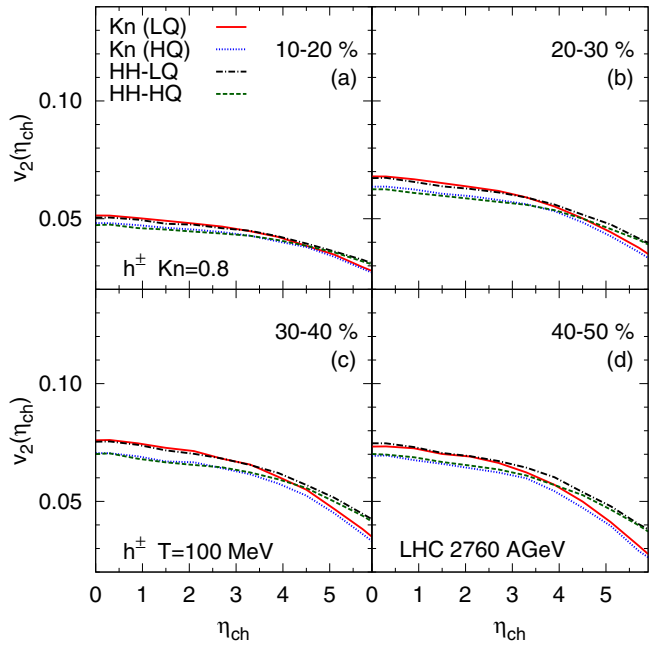

FIG. 30. (Color online) Charged hadron $v_2(\eta_{\rm ch})$ at the LHC obtained by using two different freeze-out criteria. Experimental data are from the ALICE Collaboration [75].

As a function of pseudorapidity v_2 shows more sensitivity to the freeze-out criterion (see Figs. 29 and 30). At both the RHIC and the LHC $v_2(\eta_{\rm ch})$ drops faster with increasing rapidity, when the dynamical freeze-out criterion is used. Also, with both freeze-out criteria the sensitivity to plasma viscosity disappears at large rapidities even at the LHC. This is again a manifestation of previously seen behavior: At large rapidities at the LHC, the system behaves like the system at the RHIC.

The rather weak dependence of anisotropies on the decoupling criterion means that at midrapidity fluid dynamical results are surprisingly robust against variations in the decoupling procedure. As well, this gives a reason to expect that the hybrid model results are sensitive only to the value of the switching criterion from fluid to cascade, not to the criterion itself. Since the fluid-dynamical results concerning the viscosity of the QGP are based on the analysis of anisotropies at midrapidity, this means that those results are not compromised by the freeze-out criterion. On the other hand, the sensitivity to the freeze-out description at high rapidities indicates that at lower collision energies the fluid-dynamical results may be sensitive to the freeze-out criterion even at midrapidity. Thus one has to pay extra attention to the freeze-out description of the collisions at $\sqrt{s_{\rm NN}} = 3$–9 GeV in the future Facility for Antiproton and Ion Research (FAIR) and Nuclotron-based Ion Collider Facility (NICA).

VII. CONCLUSIONS

We have studied the effects of temperature-dependent η_s/s on the azimuthal anisotropies of hadron transverse momentum spectra using genuinely (3+1)-dimensional viscous hydrodynamics. We have extended our previous studies [11,13] to backward and forward rapidities and explored the resolving power of differential measurements of v_2 and v_4 to distinguish between different parametrizations of $(\eta_s/s)(T)$.

In close to central collisions at the LHC energy, $\sqrt{s_{\rm NN}} = 2.76$ TeV, viscous suppression of elliptic flow at midrapidity is affected by both hadronic and QGP viscosities, but when one moves toward backward and forward rapidities, hadronic viscosity becomes more and more dominant—the system becomes effectively smaller and begins to behave like in collisions at the RHIC, $\sqrt{s_{\rm NN}} = 200$ GeV. Therefore, with large hadronic viscosity, v_2 tends to drop slightly faster with increasing rapidity, the effect being stronger in peripheral collisions. At both energies and at all rapidities v_4 is mostly suppressed by hadronic viscosity, but if we simultaneously change the minimum value of η_s/s, hadronic, and QGP viscosities, it is difficult to predict which coefficient at which collision energy is most sensitive to the changes. Nevertheless, the differential measurements of v_n as functions of transverse momentum, rapidity, centrality, and collision energy provide a way to distinguish different parametrizations of $(\eta_s/s)(T)$ and thus constrain the temperature dependence of the η_s/s ratio.

We also studied how sensitive our results are to the freeze-out criterion, and we found that, once the freeze-out parameters are fixed to reproduce p_T distributions, both decoupling at constant temperature and at constant Knudsen number lead to very similar anisotropies at midrapidity. Toward the large rapidities, v_2 tends to drop faster with the dynamical freeze-out criterion. This indicates that uncertainties in the decoupling description do not affect the present fluid-dynamical results regarding the anisotropies, but at lower collision energies the results may be more sensitive to the freeze-out criterion.

ACKNOWLEDGMENTS

This work was supported by the Helmholtz International Center for FAIR within the framework of the LOEWE program launched by the State of Hesse. The work of H. Niemi was supported by Academy of Finland Project No. 133005, the work of P. Huovinen by BMBF under Contract No. 06FY9092, and the work of H. Holopainen by the ExtreMe Matter Institute (EMMI). E. Molnár was partially supported by the European Union and the European Social Fund through project Supercomputer, the national virtual laboratory (Grant No. TAMOP-4.2.2.C-11/1/KONV-2012-0010), as well as by TAMOP 4.2.4.A/2-11-1-2012-0001 National Excellence Program (A2-MZPDÖ-13-0042).

APPENDIX A: EQUATIONS IN 3+1 DIMENSIONS

In the following, the components of four-vectors and tensors of rank-2 in four-dimensional space-time are denoted by Greek indices that take values from 0 to 3 while Roman indices range from 1 to 3. If not stated otherwise the Einstein summation convention for both Greek and Roman indices is implied.

First we recall the definitions of the covariant derivative of contravariant four-vectors and tensors of rank-2:

$$A^{\mu}_{;\alpha} = \partial_\alpha A^\mu + \Gamma^\mu_{\alpha\beta} A^\beta, \tag{A1}$$

$$A^{\mu\nu}_{;\alpha} = \partial_\alpha A^{\mu\nu} + \Gamma^\mu_{\alpha\beta} A^{\beta\nu} + \Gamma^\nu_{\alpha\beta} A^{\mu\beta}, \tag{A2}$$

where $\Gamma^\mu_{\alpha\beta} \equiv \Gamma^\mu_{\beta\alpha} = \frac{1}{2} g^{\mu\nu}(\partial_\beta g_{\alpha\nu} + \partial_\alpha g_{\nu\beta} - \partial_\nu g_{\alpha\beta})$ denotes the Christoffel symbol of the second kind and $\partial_\alpha = \partial/\partial x^\alpha$ denotes the four-derivative. For scalar quantities the covariant derivative reduces to the ordinary four-derivative, i.e., $(A^\mu A_\mu)_{;\alpha} = \partial_\alpha (A^\mu A_\mu)$.

Applying the definition of the transverse projection operator $\Delta^{\mu\nu} = g^{\mu\nu} - u^\mu u^\nu$ we can decompose the covariant derivative as the sum of the covariant time derivative D and spatial gradient ∇_α,

$$D A^{\mu_1 \cdots \mu_n} = u^\beta A^{\mu_1 \cdots \mu_n}_{;\beta}, \tag{A3}$$

$$\nabla_\alpha A^{\mu_1 \cdots \mu_n} = \Delta^\beta_\alpha A^{\mu_1 \cdots \mu_n}_{;\beta}; \tag{A4}$$

hence $A^{\mu_1 \cdots \mu_n}_{;\alpha} = u_\alpha D A^{\mu_1 \cdots \mu_n} + \nabla_\alpha A^{\mu_1 \cdots \mu_n}$, while for later use we also introduce the comoving or convective time derivative

$$d A^{\mu_1 \cdots \mu_n} = u^\beta \partial_\beta A^{\mu_1 \cdots \mu_n}. \tag{A5}$$

In the following, we summarize the equations of relativistic dissipative fluid dynamics in hyperbolic coordinates [i.e., (τ, x, y, η) coordinates] [57], where $\tau = (t^2 - z^2)^{-1/2}$ is the longitudinal proper time and $\eta = 1/2 \ln[(t+z)/(t-z)]$ is the space-time rapidity. The proper metric tensors are $g^{\mu\nu} = \mathrm{diag}(1, -1, -1, -\tau^{-2})$ and $g_{\mu\nu} = \mathrm{diag}(1, -1, -1, -\tau^2)$. Thus the only nonvanishing Christoffel symbols are $\Gamma^\eta_{\eta\tau} \equiv \Gamma^\eta_{\tau\eta} = \tau^{-1}$ and $\Gamma^\tau_{\eta\eta} = \tau$, and the gradient is $\partial_\mu = (\partial_\tau, \partial_x, \partial_y, \partial_\eta)$ while $\partial^\mu \equiv g^{\mu\nu}\partial_\nu = (\partial_\tau, -\partial_x, -\partial_y, -\tau^{-2}\partial_\eta)$. The inverse transformations to Minkowski coordinates with $g^{\mu\nu}_M \equiv \eta^{\mu\nu} = \mathrm{diag}(1, -1, -1, -1)$ are $t = \tau \cosh\eta$ and $z = \tau \sinh\eta$. Note that the hyperbolic coordinates are similar to the Milne coordinates that are spherically symmetric, i.e., $r \equiv \sqrt{x^2 + y^2 + z^2} = \tau \sinh\eta$.

The contravariant flow velocity is

$$u^\mu = \gamma(1, v_x, v_y, v_\eta); \tag{A6}$$

hence the covariant flow velocity is $u_\mu \equiv g_{\mu\nu} u^\nu = \gamma(1, -v_x, -v_y, -\tau^2 v_\eta)$, where the normalization condition $u^\mu u_\nu = 1$ leads to $\gamma = (1 - v_x^2 - v_y^2 - \tau^2 v_\eta^2)^{-1/2}$ as well as to $u^\mu u_{\mu;\nu} \equiv u_\mu u^\mu_{;\nu} = 0$.

The energy-momentum conservation equation in general coordinates is

$$T^{\mu\nu}_{;\mu} \equiv \frac{1}{\sqrt{g}} \partial_\mu (\sqrt{g}\, T^{\mu\nu}) + \Gamma^\nu_{\mu\beta} T^{\mu\beta} = 0, \tag{A7}$$

where $g \equiv -\det(g_{\mu\nu})$ is the negative determinant of the metric tensor, which in hyperbolic coordinates leads to $g = \tau^2$.

Henceforth the energy conservation equation leads to

$$\begin{aligned} &\partial_\tau T^{\tau\tau} + \partial_x(v_x T^{\tau\tau}) + \partial_y(v_y T^{\tau\tau}) + \partial_\eta(v_\eta T^{\tau\tau}) \\ &\quad = -\partial_x(v_x P - v_x \pi^{\tau\tau} + \pi^{\tau x}) - \partial_y(v_y P - v_y \pi^{\tau\tau} + \pi^{\tau y}) \\ &\qquad -\partial_\eta(v_\eta P - v_\eta \pi^{\tau\tau} + \pi^{\tau\eta}) - \frac{1}{\tau}(T^{\tau\tau} + \tau^2 T^{\eta\eta}), \end{aligned} \tag{A8}$$

while the momentum-conservation equation leads to

$$\begin{aligned} &\partial_\tau T^{\tau x} + \partial_x(v_x T^{\tau x}) + \partial_y(v_y T^{\tau x}) + \partial_\eta(v_\eta T^{\tau x}) \\ &\quad = -\partial_x(P - v_x \pi^{\tau x} + \pi^{xx}) - \partial_y(-v_y \pi^{\tau x} + \pi^{xy}) \\ &\qquad -\partial_\eta(-v_\eta \pi^{\tau x} + \pi^{x\eta}) - \frac{1}{\tau} T^{\tau x}, \end{aligned} \tag{A9}$$

$$\begin{aligned} &\partial_\tau T^{\tau y} + \partial_x(v_x T^{\tau y}) + \partial_y(v_y T^{\tau y}) + \partial_\eta(v_\eta T^{\tau y}) \\ &\quad = -\partial_x(-v_x \pi^{\tau y} + \pi^{xy}) - \partial_y(P - v_y \pi^{\tau y} + \pi^{yy}) \\ &\qquad -\partial_\eta(-v_\eta \pi^{\tau y} + \pi^{y\eta}) - \frac{1}{\tau} T^{\tau y}, \end{aligned} \tag{A10}$$

$$\begin{aligned} &\partial_\tau T^{\tau\eta} + \partial_x(v_x T^{\tau\eta}) + \partial_y(v_y T^{\tau\eta}) + \partial_\eta(v_\eta T^{\tau\eta}) \\ &\quad = -\partial_x(-v_x \pi^{\tau\eta} + \pi^{x\eta}) - \partial_y(-v_y \pi^{\tau\eta} + \pi^{y\eta}) \\ &\qquad -\partial_\eta\left(\frac{P}{\tau^2} - v_\eta \pi^{\tau\eta} + \pi^{\eta\eta}\right) - \frac{3}{\tau} T^{\tau\eta}. \end{aligned} \tag{A11}$$

The corresponding tensor components are defined according to the general definition of the energy-momentum tensor [Eq. (2)]:

$$T^{\tau\tau} = (e + P)\gamma^2 - g^{\tau\tau} P + \pi^{\tau\tau}, \tag{A12}$$

$$\begin{aligned} T^{\tau i} &\equiv (e + P)\gamma^2 v_i - g^{\tau i} P + \pi^{\tau i}, \\ &= v_i T^{\tau\tau} + P(g^{\tau\tau} v_i - g^{\tau i}) - v_i \pi^{\tau\tau} + \pi^{\tau i}, \end{aligned} \tag{A13}$$

$$\begin{aligned} T^{ij} &\equiv (e + P)\gamma^2 v_i v_j - P g^{ij} + \pi^{ij}, \\ &= v_i T^{\tau j} + P(g^{\tau j} v_i - g^{ij}) - v_i \pi^{\tau j} + \pi^{ij}. \end{aligned} \tag{A14}$$

A simplified but mathematically equivalent way of writing the equations of motion can be obtained by introducing scaled variables that absorb the $\sqrt{g}$ factor [76],

$$\tilde{T}^{\mu\nu} = \tau T^{\mu\nu}; \tag{A15}$$

hence we are led to the following τ-scaled equations:

$$\partial_\mu \tilde{T}^{\tau\mu} = -\tau \tilde{T}^{\eta\eta}, \tag{A16}$$

$$\partial_\mu \tilde{T}^{x\mu} = 0, \quad \partial_\mu \tilde{T}^{y\mu} = 0, \quad \partial_\mu \tilde{T}^{\eta\mu} = -\frac{2}{\tau} \tilde{T}^{\tau\eta}. \tag{A17}$$

For example, in special test cases with no transverse pressure and vanishing dissipation we can solve the energy-conservation equation exactly. We found that by solving the scaled equations we can achieve approximately $\mathcal{O}_5$ numerical precision, which is in comparison about two orders of magnitude more accurate than the numerical solution of the nonscaled equations of motion using the same time step. Note that the τ scaling from Eq. (A15) also affects the relaxation equations for the shear-stress tensor. Therefore the scaled quantities $\tilde{\pi}^{\mu\nu} = \tau \pi^{\mu\nu}$ result in $d\tilde{\pi}^{\mu\nu} - \tilde{\pi}^{\mu\nu}/\tau = \tau d\pi^{\mu\nu}$.

For a better understanding of what will follow, we introduce the notation $u^\mu = \gamma(1, \bar{\mathbf{v}}_i)$ for the contravariant flow velocity from Eq. (A6). Similarly, the covariant component is denoted as $u_\mu = \gamma(1, -\underline{\mathbf{v}}_i)$; thus $v^2 \equiv \bar{\mathbf{v}}_i \underline{\mathbf{v}}_i = v_x^2 + v_y^2 + \tau^2 v_\eta^2$ and $\gamma = \sqrt{1 - v^2}$.

In our case of interest, $g^{\tau\tau} = 1$, and the metric of space-time is diagonal, leading to $g^{\tau i} = 0$; thus we can introduce a simplified notation which mimics the ideal fluid relations, $E \equiv T^{\tau\tau} - \pi^{\tau\tau} = T_{\tau\tau} - \pi_{\tau\tau}$, $\bar{M}_i \equiv T^{\tau i} - \pi^{\tau i}$, and $\underline{\mathrm{M}}_i \equiv T_{\tau i} - \pi_{\tau i} = g_{\alpha\tau} g_{\beta i}(T^{\alpha\beta} - \pi^{\alpha\beta})$. Using this notation we obtain the

local rest frame energy density from Eqs. (A12) and (A13):

$$e \equiv T^{\tau\tau} - \pi^{\tau\tau} - (T^{\tau i} - \pi^{\tau i})\underline{\mathbf{v}}_i = E - \bar{M}_i \underline{\mathbf{v}}_i, \tag{A18}$$

while the expression for the velocity components from Eq. (A13) leads to

$$\bar{\mathbf{v}}_i \equiv \frac{T^{\tau i} - \pi^{\tau i}}{T^{\tau\tau} - \pi^{\tau\tau} + P} = \frac{\bar{M}_i}{E + P}. \tag{A19}$$

Now, similarly expressing the $\underline{\mathbf{v}}_i$ components we define the magnitude of the three-velocity as

$$v \equiv \sqrt{\bar{\mathbf{v}}_i \underline{\mathbf{v}}_i} = \frac{M}{E + P}, \tag{A20}$$

where $M \equiv (\bar{M}_i \underline{\mathrm{M}}_i)^{1/2} = \sqrt{\bar{M}_x^2 + \bar{M}_y^2 + \tau^2 \bar{M}_\eta^2}$. Using the latter two equations together we obtain

$$\bar{\mathbf{v}}_i = v \frac{\bar{M}_i}{M}. \tag{A21}$$

Therefore, with the help of Eq. (A18), Eq. (A20) can be solved by using a one-dimensional root search, whereas Eq. (A21) yields the individual velocity components.

In general, we can reduce the number of unknowns in the relaxation equations (4) by applying the orthogonality and tracelessness conditions of the shear-stress tensor. For example, by choosing π^{xx}, π^{yy}, π^{xy}, $\pi^{x\eta}$, and $\pi^{y\eta}$ as independent components, the other four components of the shear-stress tensor follow from the orthogonality $\pi^{\mu\nu} u_\nu = 0$:

$$\pi^{\tau\tau} = \pi^{\tau x} v_x + \pi^{\tau y} v_y + \tau^2 \pi^{\tau\eta} v_\eta, \tag{A22}$$

$$\pi^{\tau x} = \pi^{xx} v_x + \pi^{xy} v_y + \tau^2 \pi^{x\eta} v_\eta, \tag{A23}$$

$$\pi^{\tau y} = \pi^{xy} v_x + \pi^{yy} v_y + \tau^2 \pi^{y\eta} v_\eta, \tag{A24}$$

$$\pi^{\tau\eta} = \pi^{x\eta} v_x + \pi^{y\eta} v_y + \tau^2 \pi^{\eta\eta} v_\eta, \tag{A25}$$

whereas the last unknown component is available from the tracelessness condition $\pi^{\mu\nu} g_{\mu\nu} = 0$:

$$\begin{aligned}\pi^{\eta\eta} &\equiv \tau^{-2}(\pi^{\tau\tau} - \pi^{xx} - \pi^{yy}) \\ &= \tau^{-2}\left[\pi^{xx}\left(v_x^2 - 1\right) + \pi^{yy}\left(v_y^2 - 1\right) + 2\pi^{xy} v_x v_y \right. \\ &\quad \left. + 2\tau^2(\pi^{x\eta} v_x v_\eta + \pi^{y\eta} v_y v_\eta)\right] \big/ \left(1 - \tau^2 v_\eta^2\right).\end{aligned} \tag{A26}$$

Note that solving the above algebraic equations to obtain the remaining five components, instead of explicitly propagating all ten components of the shear-stress tensor, we introduce a small numerical error compared to the latter method. This is because the velocities entering into Eqs. (A22)–(A26) are given from the previous (half) time step, so we obtain different values with different methods. However, this difference usually becomes smaller as the number of time steps increases; hence this small numerical error is acceptable especially if the runtime is also reduced considerably.

For sake of completeness we write out all terms from the shear-stress relaxation equations explicitly. The relaxation equations for the chosen five independent components of the shear-stress tensor π^{xx}, π^{yy}, π^{xy}, $\pi^{x\eta}$, and $\pi^{y\eta}$ are

$$\tau_\pi d\pi^{xx} = 2\eta_s \sigma^{xx} - \pi^{xx} - I^{xx}, \tag{A27}$$

$$\tau_\pi d\pi^{yy} = 2\eta_s \sigma^{yy} - \pi^{yy} - I^{yy}, \tag{A28}$$

$$\tau_\pi d\pi^{xy} = 2\eta_s \sigma^{xy} - \pi^{xy} - I^{xy}, \tag{A29}$$

$$\tau_\pi d\pi^{x\eta} = 2\eta_s \sigma^{x\eta} - \pi^{x\eta} - \tau_\pi \frac{\gamma}{\tau}(\pi^{x\eta} + v_\eta \pi^{\tau x}) - I^{x\eta}, \tag{A30}$$

$$\tau_\pi d\pi^{y\eta} = 2\eta_s \sigma^{y\eta} - \pi^{y\eta} - \tau_\pi \frac{\gamma}{\tau}(\pi^{y\eta} + v_\eta \pi^{\tau y}) - I^{y\eta}. \tag{A31}$$

Here according to Eq. (4) we denoted

$$I^{\mu\nu} = I_1^{\mu\nu} + \delta_{\pi\pi} I_2^{\mu\nu} - \tau_\pi I_3^{\mu\nu} + \tau_{\pi\pi} I_4^{\mu\nu} - \varphi_7 I_5^{\mu\nu}, \tag{A32}$$

where

$$I_1^{\mu\nu} = (\pi^{\lambda\mu} u^\nu + \pi^{\lambda\nu} u^\mu) Du_\lambda, \tag{A33}$$

$$I_2^{\mu\nu} = \theta \pi^{\mu\nu}, \tag{A34}$$

$$I_3^{\mu\nu} = \pi^{\mu\lambda} \omega_\lambda^\nu + \pi^{\nu\lambda} \omega_\lambda^\mu, \tag{A35}$$

$$I_4^{\mu\nu} = \tfrac{1}{2} g_{\lambda\kappa}(\pi^{\mu\kappa}\sigma^{\nu\lambda} + \pi^{\nu\kappa}\sigma^{\mu\lambda}) - \tfrac{1}{3}\Delta^{\mu\nu}\pi_\beta^\alpha \sigma_\alpha^\beta, \tag{A36}$$

$$I_5^{\mu\nu} = g_{\lambda\kappa}\pi^{\mu\kappa}\pi^{\nu\lambda} - \tfrac{1}{3}\Delta^{\mu\nu}\pi_\beta^\alpha \pi_\alpha^\beta. \tag{A37}$$

The I_1 terms are

$$I_1^{xx} = 2\gamma v_x(\pi^{\tau x} Du_\tau + \pi^{xx} Du_x + \pi^{yx} Du_y + \pi^{\eta x} Du_\eta), \tag{A38}$$

$$I_1^{yy} = 2\gamma v_y(\pi^{\tau y} Du_\tau + \pi^{xy} Du_x + \pi^{yy} Du_y + \pi^{\eta y} Du_\eta), \tag{A39}$$

$$\begin{aligned} I_1^{xy} = \gamma[&(\pi^{\tau x} v_y + \pi^{\tau y} v_x) Du_\tau + (\pi^{xx} v_y + \pi^{xy} v_x) Du_x \\ &+ (\pi^{yx} v_y + \pi^{yy} v_x) Du_y + (\pi^{\eta x} v_y + \pi^{\eta y} v_x) Du_\eta], \end{aligned} \tag{A40}$$

$$\begin{aligned} I_1^{x\eta} = \gamma[&(\pi^{\tau x} v_\eta + \pi^{\tau\eta} v_x) Du_\tau + (\pi^{xx} v_\eta + \pi^{x\eta} v_x) Du_x \\ &+ (\pi^{yx} v_\eta + \pi^{y\eta} v_x) Du_y + (\pi^{\eta x} v_\eta + \pi^{\eta\eta} v_x) Du_\eta], \end{aligned} \tag{A41}$$

$$\begin{aligned} I_1^{y\eta} = \gamma[&(\pi^{\tau y} v_\eta + \pi^{\tau\eta} v_y) Du_\tau + (\pi^{xy} v_\eta + \pi^{x\eta} v_y) Du_x \\ &+ (\pi^{yy} v_\eta + \pi^{y\eta} v_y) Du_y + (\pi^{\eta y} v_\eta + \pi^{\eta\eta} v_y) Du_\eta], \end{aligned} \tag{A42}$$

where according to Eqs. (A3) and (A5) the proper time derivatives are given by $Du_\mu = du_\mu - \Gamma^\beta_{\mu\alpha} u^\alpha u_\beta$ and hence

$$Du_\tau \equiv Du^\tau = \gamma[\partial_\tau \gamma + v_x \partial_x \gamma + v_y \partial_y \gamma + v_\eta \partial_\eta \gamma] + \tau \gamma^2 v_\eta^2, \tag{A43}$$

$$\begin{aligned} Du_x \equiv -Du^x = -\gamma[&\partial_\tau(\gamma v_x) + v_x \partial_x(\gamma v_x) \\ &+ v_y \partial_y(\gamma v_x) + v_\eta \partial_\eta(\gamma v_x)], \end{aligned} \tag{A44}$$

$$\begin{aligned} Du_y \equiv -Du^y = -\gamma[&\partial_\tau(\gamma v_y) + v_x \partial_x(\gamma v_y) \\ &+ v_y \partial_y(\gamma v_y) + v_\eta \partial_\eta(\gamma v_y)], \end{aligned} \tag{A45}$$

$$\begin{aligned} Du_\eta \equiv -\tau^2 Du^\eta = -\gamma\tau^2[&\partial_\tau(\gamma v_\eta) + v_x \partial_x(\gamma v_\eta) \\ &+ v_y \partial_y(\gamma v_\eta) + v_\eta \partial_\eta(\gamma v_\eta)] - 2\tau\gamma^2 v_\eta. \end{aligned} \tag{A46}$$

Note that $Du_\tau \equiv du_\tau + \tau\gamma^2 v_\eta^2 = du^\tau + \tau\gamma^2 v_\eta^2$, $Du_x \equiv du_x = -du^x$, $Du_y \equiv du_y = -du^y$, and $Du_\eta \equiv du_\eta \neq du^\eta$, since $Du^\eta \equiv du^\eta + 2\tau^{-1}\gamma^2 v_\eta = -\tau^2 du_\eta$.

The I_3 terms are

$$I_3^{xx} = 2\left(\pi^{x\tau}\omega^x{}_\tau + \pi^{xy}\omega^x{}_y + \pi^{x\eta}\omega^x{}_\eta\right), \tag{A47}$$

$$I_3^{yy} = 2\left(\pi^{y\tau}\omega^y{}_\tau + \pi^{yx}\omega^y{}_x + \pi^{y\eta}\omega^y{}_\eta\right), \tag{A48}$$

$$I_3^{xy} = \pi^{x\tau}\omega^y{}_\tau + \pi^{y\tau}\omega^x{}_\tau + \pi^{xx}\omega^y{}_x + \pi^{yy}\omega^x{}_y + \pi^{x\eta}\omega^y{}_\eta + \pi^{y\eta}\omega^x{}_\eta, \tag{A49}$$

$$I_3^{x\eta} = \pi^{x\tau}\omega^\eta{}_\tau + \pi^{\eta\tau}\omega^x{}_\tau + \pi^{xx}\omega^\eta{}_x + \pi^{xy}\omega^\eta{}_y + \pi^{\eta y}\omega^x{}_y + \pi^{\eta\eta}\omega^x{}_\eta, \tag{A50}$$

$$I_3^{y\eta} = \pi^{y\tau}\omega^\eta{}_\tau + \pi^{\eta\tau}\omega^y{}_\tau + \pi^{yx}\omega^\eta{}_x + \pi^{\eta x}\omega^y{}_x + \pi^{yy}\omega^\eta{}_y + \pi^{\eta\eta}\omega^y{}_\eta, \tag{A51}$$

where the vorticities are defined most generally as

$$\begin{aligned}\omega^\mu{}_\nu &\equiv \tfrac{1}{2}\Delta^{\mu\alpha}\Delta^\beta{}_\nu(u_{\alpha;\beta} - u_{\beta;\alpha}) \\ &= \tfrac{1}{2}\left[g^{\mu\alpha}\left(\partial_\nu u_\alpha - u_\nu du_\alpha\right) - g^\beta_\nu(\partial^\mu u_\beta - u^\mu du_\beta)\right] \\ &\quad + \tfrac{1}{2}(g^{\mu\alpha}u_\nu - g^\alpha{}_\nu u^\mu)u^\beta\Gamma^\lambda_{\alpha\beta}u_\lambda.\end{aligned} \tag{A52}$$

Here we used the fact that the Christoffel symbols of the second kind are symmetric, $\Gamma^\mu_{\alpha\beta} = \Gamma^\mu_{\beta\alpha}$, with respect to the interchange of the two lower indices.

The different components of the vorticity are given as

$$\begin{aligned}\omega^\tau{}_x \equiv \omega^x{}_\tau &= \tfrac{1}{2}[\partial_\tau(\gamma v_x) + \partial_x\gamma] \\ &\quad + \tfrac{1}{2}\left[\gamma v_x d\gamma - \gamma d\left(\gamma v_x\right)\right] + \tfrac{1}{2}\tau\gamma^3 v_\eta^2 v_x,\end{aligned} \tag{A53}$$

$$\begin{aligned}\omega^\tau{}_y \equiv \omega^y{}_\tau &= \tfrac{1}{2}[\partial_\tau(\gamma v_y) + \partial_y\gamma] \\ &\quad + \tfrac{1}{2}[\gamma v_y d\gamma - \gamma d(\gamma v_y)] + \tfrac{1}{2}\tau\gamma^3 v_\eta^2 v_y,\end{aligned} \tag{A54}$$

$$\begin{aligned}\omega^\tau{}_\eta \equiv \tau^2\omega^\eta{}_\tau &= \tfrac{1}{2}[\partial_\tau(\tau^2\gamma v_\eta) + \partial_\eta\gamma] \\ &\quad + \tfrac{1}{2}[\tau^2\gamma v_\eta d\gamma - \gamma d(\tau^2\gamma v_\eta)] + \tfrac{1}{2}\tau^3\gamma^3 v_\eta^3\end{aligned} \tag{A55}$$

and

$$\begin{aligned}\omega^x{}_y \equiv -\omega^y{}_x &= \tfrac{1}{2}[\partial_y(\gamma v_x) - \partial_x(\gamma v_y)] \\ &\quad + \tfrac{1}{2}[\gamma v_y d(\gamma v_x) - \gamma v_x d(\gamma v_y)],\end{aligned} \tag{A56}$$

$$\begin{aligned}\omega^x{}_\eta \equiv -\tau^2\omega^\eta{}_x &= \tfrac{1}{2}[\partial_\eta(\gamma v_x) - \partial_x(\tau^2\gamma v_\eta)] \\ &\quad + \tfrac{1}{2}[\tau^2\gamma v_\eta d(\gamma v_x) - \gamma v_x d(\tau^2\gamma v_\eta)],\end{aligned} \tag{A57}$$

$$\begin{aligned}\omega^y{}_\eta \equiv -\tau^2\omega^\eta{}_y &= \tfrac{1}{2}[\partial_\eta(\gamma v_y) - \partial_y(\tau^2\gamma v_\eta)] \\ &\quad + \tfrac{1}{2}[\tau^2\gamma v_\eta d(\gamma v_y) - \gamma v_y d(\tau^2\gamma v_\eta)].\end{aligned} \tag{A58}$$

Note that the general expression of the vorticity given in Eq. (10) in Ref. [77] is missing the contribution of the Christoffel symbols compared to Eq. (A52) in this work. Therefore, the values for $\omega^\tau{}_x$, $\omega^\tau{}_y$, and $\omega^\tau{}_\eta$ given in Eqs. (C.22), (C.23), and (C.24) in Ref. [77] are also incorrect compared to these formulas.

The next term we need is given by

$$\begin{aligned}I_4^{xx} &= (\pi^{x\tau}\sigma^{x\tau} - \pi^{xx}\sigma^{xx} - \pi^{xy}\sigma^{xy} - \tau^2\pi^{x\eta}\sigma^{x\eta}) \\ &\quad + \frac{1}{3}\left(1 + \gamma^2 v_x^2\right)\pi^\alpha_\beta\sigma^\beta_\alpha,\end{aligned} \tag{A59}$$

$$\begin{aligned}I_4^{yy} &= \pi^{y\tau}\sigma^{y\tau} - \pi^{yx}\sigma^{yx} - \pi^{yy}\sigma^{yy} - \tau^2\pi^{y\eta}\sigma^{y\eta} \\ &\quad + \frac{1}{3}\left(1 + \gamma^2 v_y^2\right)\pi^\alpha_\beta\sigma^\beta_\alpha,\end{aligned} \tag{A60}$$

$$\begin{aligned}I_4^{xy} &= \frac{1}{2}(\pi^{x\tau}\sigma^{y\tau} + \pi^{y\tau}\sigma^{x\tau}) - \frac{1}{2}(\pi^{xx}\sigma^{yx} + \pi^{yx}\sigma^{xx}) \\ &\quad - \frac{1}{2}\left(\pi^{xy}\sigma^{yy} + \pi^{yy}\sigma^{xy}\right) - \frac{\tau^2}{2}(\pi^{x\eta}\sigma^{y\eta} + \pi^{y\eta}\sigma^{x\eta}) \\ &\quad + \frac{1}{3}\left(\gamma^2 v_x v_y\right)\pi^\alpha_\beta\sigma^\beta_\alpha,\end{aligned} \tag{A61}$$

$$\begin{aligned}I_4^{x\eta} &= \frac{1}{2}(\pi^{x\tau}\sigma^{\eta\tau} + \pi^{\eta\tau}\sigma^{x\tau}) - \frac{1}{2}(\pi^{xx}\sigma^{\eta x} + \pi^{\eta x}\sigma^{xx}) \\ &\quad - \frac{1}{2}(\pi^{xy}\sigma^{\eta y} + \pi^{\eta y}\sigma^{xy}) - \frac{\tau^2}{2}(\pi^{x\eta}\sigma^{\eta\eta} + \pi^{\eta\eta}\sigma^{x\eta}) \\ &\quad + \frac{1}{3}(\gamma^2 v_x v_\eta)\pi^\alpha_\beta\sigma^\beta_\alpha,\end{aligned} \tag{A62}$$

$$\begin{aligned}I_4^{y\eta} &= \frac{1}{2}(\pi^{y\tau}\sigma^{\eta\tau} + \pi^{\eta\tau}\sigma^{y\tau}) - \frac{1}{2}(\pi^{yx}\sigma^{\eta x} + \pi^{\eta x}\sigma^{yx}) \\ &\quad - \frac{1}{2}(\pi^{yy}\sigma^{\eta y} + \pi^{\eta y}\sigma^{yy}) - \frac{\tau^2}{2}(\pi^{y\eta}\sigma^{\eta\eta} + \pi^{\eta\eta}\sigma^{y\eta}) \\ &\quad + \frac{1}{3}(\gamma^2 v_y v_\eta)\pi^\alpha_\beta\sigma^\beta_\alpha.\end{aligned} \tag{A63}$$

The shear tensor is most generally defined as

$$\begin{aligned}\sigma^{\mu\nu} \equiv \nabla^{\langle\mu}u^{\nu\rangle} &= \frac{1}{2}\Delta^{\mu\alpha}\Delta^{\nu\beta}(u_{\alpha;\beta} + u_{\beta;\alpha}) - \frac{\theta}{3}\Delta^{\mu\nu} \\ &= \frac{1}{2}[g^{\mu\alpha}(\partial^\nu u_\alpha - u^\nu du_\alpha) + g^{\nu\beta}(\partial^\mu u_\beta - u^\mu du_\beta)] \\ &\quad - \Delta^{\mu\alpha}\Delta^{\nu\beta}\Gamma^\lambda_{\alpha\beta}u_\lambda - \frac{\theta}{3}\Delta^{\mu\nu},\end{aligned} \tag{A64}$$

whereas the expansion scalar is

$$\begin{aligned}\theta \equiv \nabla_\mu u^\mu &= \partial_\mu u^\mu + \Gamma^\lambda_{\lambda\mu}u^\mu \\ &= \frac{\gamma}{\tau} + \partial_\tau\gamma + \partial_x(\gamma v_x) + \partial_y(\gamma v_y) + \partial_\eta(\gamma v_\eta).\end{aligned} \tag{A65}$$

The various shear tensor components that we need to use are

$$\sigma^{\tau\tau} = -\tau\gamma^3 v_\eta^2 + [(\partial_\tau\gamma - \gamma d\gamma)] + (\gamma^2 - 1)\frac{\theta}{3}, \tag{A66}$$

$$\begin{aligned}\sigma^{\tau x} &= -\frac{1}{2}\left(\tau\gamma^3 v_\eta^2 v_x\right) + \frac{1}{2}\left[\partial_\tau\left(\gamma v_x\right) - \partial_x\gamma\right] \\ &\quad - \frac{1}{2}\left[\gamma v_x d\gamma + \gamma d\left(\gamma v_x\right)\right] + \gamma^2 v_x\frac{\theta}{3},\end{aligned} \tag{A67}$$

$$\begin{aligned}\sigma^{\tau y} &= -\frac{1}{2}\left(\tau\gamma^3 v_\eta^2 v_y\right) + \frac{1}{2}[\partial_\tau(\gamma v_y) - \partial_y\gamma] \\ &\quad - \frac{1}{2}[\gamma v_y d\gamma + \gamma d(\gamma v_y)] + \gamma^2 v_y\frac{\theta}{3},\end{aligned} \tag{A68}$$

$$\begin{aligned}\sigma^{\tau\eta} &= -\frac{\gamma^3 v_\eta}{2\tau}\left(2 + \tau^2 v_\eta^2\right) + \frac{1}{2}\left[\partial_\tau(\gamma v_\eta) - \frac{1}{\tau^2}\partial_\eta\gamma\right] \\ &\quad - \frac{1}{2}[\gamma v_\eta d\gamma + \gamma d(\gamma v_\eta)] + \gamma^2 v_\eta\frac{\theta}{3},\end{aligned} \tag{A69}$$

$$\sigma^{\eta\eta} = -\frac{\gamma}{\tau^3}\left(1+2\tau^2\gamma^2 v_\eta^2\right) - \frac{1}{\tau^2}\partial_\eta(\gamma v_\eta) - (\gamma v_\eta) d(\gamma v_\eta) + \left(\frac{1}{\tau^2}+\gamma^2 v_\eta^2\right)\frac{\theta}{3} \tag{A70}$$

and

$$\sigma^{xx} = -\left[\partial_x(\gamma v_x) + \gamma v_x d(\gamma v_x)\right] + \left(1+\gamma^2 v_x^2\right)\frac{\theta}{3}, \tag{A71}$$

$$\sigma^{yy} = -\left[\partial_y(\gamma v_y) + \gamma v_y d(\gamma v_y)\right] + \left(1+\gamma^2 v_y^2\right)\frac{\theta}{3}, \tag{A72}$$

$$\sigma^{xy} = -\frac{1}{2}\left[\partial_x(\gamma v_y) + \partial_y(\gamma v_x)\right] - \frac{1}{2}\left[\gamma v_y d(\gamma v_x) + \gamma v_x d(\gamma v_y)\right] + \gamma^2 v_x v_y \frac{\theta}{3}, \tag{A73}$$

$$\sigma^{x\eta} = -\frac{\gamma^3 v_x v_\eta}{\tau} - \frac{1}{2}\left[\partial_x(\gamma v_\eta) + \frac{1}{\tau^2}\partial_\eta(\gamma v_x)\right] - \frac{1}{2}\left[\gamma v_\eta d(\gamma v_x) + \gamma v_x d(\gamma v_\eta)\right] + \gamma^2 v_x v_\eta \frac{\theta}{3}, \tag{A74}$$

$$\sigma^{y\eta} = -\frac{\gamma^3 v_y v_\eta}{\tau} - \frac{1}{2}\left[\partial_y(\gamma v_\eta) + \frac{1}{\tau^2}\partial_\eta(\gamma v_y)\right] - \frac{1}{2}\left[\gamma v_\eta d(\gamma v_y) + \gamma v_y d(\gamma v_\eta)\right] + \gamma^2 v_y v_\eta \frac{\theta}{3}. \tag{A75}$$

The last contributions from Eq. (A32) are

$$I_5^{xx} = (\pi^{x\tau})^2 - (\pi^{xx})^2 - (\pi^{xy})^2 - (\tau\pi^{x\eta})^2 + \tfrac{1}{3}\left(1+\gamma^2 v_x^2\right)\pi_\beta^\alpha \pi_\alpha^\beta, \tag{A76}$$

$$I_5^{yy} = (\pi^{y\tau})^2 - (\pi^{yx})^2 - (\pi^{yy})^2 - (\tau\pi^{y\eta})^2 + \tfrac{1}{3}\left(1+\gamma^2 v_y^2\right)\pi_\beta^\alpha \pi_\alpha^\beta, \tag{A77}$$

$$I_5^{xy} = \pi^{x\tau}\pi^{y\tau} - \pi^{xx}\pi^{yx} - \pi^{xy}\pi^{yy} - \tau^2\pi^{x\eta}\pi^{y\eta} + \tfrac{1}{3}(\gamma^2 v_x v_y)\pi_\beta^\alpha \pi_\alpha^\beta, \tag{A78}$$

$$I_5^{x\eta} = \pi^{x\tau}\pi^{\eta\tau} - \pi^{xx}\pi^{\eta x} - \pi^{xy}\pi^{\eta y} - \tau^2\pi^{x\eta}\pi^{\eta\eta} + \tfrac{1}{3}(\gamma^2 v_x v_\eta)\pi_\beta^\alpha \pi_\alpha^\beta, \tag{A79}$$

$$I_5^{y\eta} = \pi^{y\tau}\pi^{\eta\tau} - \pi^{yx}\pi^{\eta x} - \pi^{yy}\pi^{\eta y} - \tau^2\pi^{y\eta}\pi^{\eta\eta} + \tfrac{1}{3}(\gamma^2 v_y v_\eta)\pi_\beta^\alpha \pi_\alpha^\beta. \tag{A80}$$

Furthermore, to evaluate the Cooper-Frye formula, Eq. (5), as well as the argument of the equilibrium distribution function, Eq. (8), we express the four-momenta of particles as

$$p^\mu = \left(m_T\cosh(y_p-\eta), p_x, p_y, \frac{m_T}{\tau}\sinh(y_p-\eta)\right), \tag{A81}$$

where m is the rest mass of the particle, $m_T = \sqrt{m^2+p_x^2+p_y^2}$ denotes the transverse mass, while y_p is the rapidity of the particle. Therefore, the nonequilibrium corrections to the spectra from Eq. (7) are given with an argument of

$$\begin{aligned}\pi^{\alpha\beta}p_\alpha p_\beta = {} & m_T^2[\cosh^2(y_p-\eta)\pi^{\tau\tau} + \tau^2\sinh^2(y_p-\eta)\pi^{\eta\eta}] \\ & +\left(p_x^2\pi^{xx} + 2p_x p_y \pi^{xy} + p_y^2\pi^{yy}\right) \\ & -2m_T\cosh(y_p-\eta)(p_x\pi^{\tau x} + p_y\pi^{\tau y}) \\ & +2\tau m_T\sinh(y_p-\eta)(p_x\pi^{x\eta} + p_y\pi^{y\eta}) \\ & -2\tau m_T^2\sinh(y_p-\eta)\cosh(y_p-\eta)\pi^{\tau\eta},\end{aligned} \tag{A82}$$

while using Eq. (C4) we obtain

$$p^\mu d^3\Sigma_\mu = \tau\Big[m_T\cosh(y_p-\eta)dxdyd\eta - p_x d\tau dyd\eta - p_y d\tau dxd\eta - \frac{m_T}{\tau}\sinh(y_p-\eta)d\tau dxdy\Big]. \tag{A83}$$

APPENDIX B: NUMERICAL METHODS

The conservation laws as well as the relaxation equations are solved using the well-known SHASTA (SHarp and Smooth Transport Algorithm) originally developed by Boris and Book [78] and later refined by Zalesak [79] and others [80]. This numerical algorithm solves equations of the conservation type with source terms:

$$\partial_t U + \partial_i(v_i U) = S(t,\mathbf{x}), \tag{B1}$$

where $U = U(t,\mathbf{x})$ is, for example, T^{00} or T^{0i}, while v_i is the ith component of three-velocity, and $S(t,\mathbf{x})$ is a source term; for more details see Refs. [77,81,82].

Because for smooth solutions (like in our case) the multidimensional antidiffusion limiter suffers from instabilities around the boundary caused by small ripples propagating into the interior [83], we further stabilized SHASTA by letting the antidiffusion coefficient $A_{\rm ad}$, which controls the amount of numerical diffusion, be proportional to

$$A_{\rm ad} = \frac{A_{\rm ad}^S}{(k/e)^2+1}, \tag{B2}$$

where $A_{\rm ad}^S = 0.125$ is the default value for the antidiffusion coefficient [78], e is the energy density in the local rest frame, and $k = 6\times10^{-5}$ GeV/fm^3 is a numerical parameter. In this way we increase the amount of numerical diffusion in the low-density region and $A_{\rm ad}$ goes smoothly to zero near the boundaries of the grid. In our cases of interest this neither affects the solution nor produces more entropy inside the decoupling surface.

It is also important to mention that in the (3+1)-dimensional case both the conservation and the relaxation equations are solved using SHASTA, employing the above-mentioned modification for the antidiffusion coefficient. Earlier, for the (2+1)-dimensional boost-invariant case, we used a simple centered second-order difference algorithm to solve the relaxation equations [13]. However doing so in the (3+1)-dimensional case does not always lead to stable solutions.

To further stabilize the numerical calculations (and also for ideal fluids) we used a smaller value for the antidiffusion coefficient in the transverse directions, $A_{\rm ad}^{x,y} = 0.105$, but kept $A_{\rm ad}^{\eta} = 0.125$ in the η direction. Decreasing the antidiffusion coefficient produces smoother solutions inside the decoupling hypersurface but also increases the numerical diffusion, which in turn may decrease the numerical accuracy. The reason we used a different coefficient in the longitudinal direction is to increase the accuracy; see the next section for more details.

The numerical calculations are done on a discretized spatial grid (including four boundary points in each direction as required by the algorithm) of $N_x \times N_y \times N_\eta$ cells with $N_x = N_y = 180$ while $N_\eta = 2 \times 120$ with $\Delta x = \Delta y = \Delta\eta = 0.15$ fm cell sizes. The time step is given from $\Delta\tau = \lambda\Delta x$, which for $\lambda = 0.4$ leads to $\Delta\tau = 0.06$ fm/c. Furthermore, the system is symmetric around the x and y directions, with exponentially interpolated boundary conditions for the conserved quantities (e.g., for Glauber-type initial conditions) and linearly interpolated boundary conditions for the shear-stress tensor (because the shear-stress tensor may change sign).

Finally, the freeze-out hypersurface is constructed at time intervals $\Delta\tau_{\rm CF} \equiv 5\Delta\tau = 0.3$ fm/c. The space is sampled uniformly in both the transverse and longitudinal directions, at $\Delta x_{\rm CF} \equiv 2\Delta x = 0.3$ fm distances.

The freeze-out hypersurface is calculated by using the CORNELIUS++ subroutine presented in Ref. [84] and its source code can be obtained from the Open Standard Codes and Routines (OSCAR) website [85].

APPENDIX C: REMARKS ON THE NUMERICAL ACCURACY

SHASTA solves the fluid dynamical equations up to some finite numerical accuracy. In most cases this means that in Cartesian coordinates the particle number and energy are conserved up to $\mathcal{O}_5$ accuracy. However, in (τ,x,y,η) coordinates, the expressions for the conserved quantities as well as the equations of motion change with additional source terms resulting from the nonvanishing Christoffel symbols.

As an example let us evaluate a conserved quantity at a given time or proper time; hence by comparing this initial value with one at a later time we can follow the accuracy of the fluid-dynamical solver during this time interval.

The total conserved charge $N_{\rm tot}$ across any given hypersurface is

$$N_{\rm tot} \equiv \int N^\mu d^3\Sigma_\mu = \int N^0 d^3\Sigma_0 + \int N^i d^3\Sigma_i. \tag{C1}$$

Here the hypersurface element $d^3\Sigma_\mu$ can be specified in any coordinate system according to the following general formula:

$$d^3\Sigma_\mu = -\epsilon_{\mu\nu\lambda\kappa}\frac{\partial\Sigma^\nu}{\partial u}\frac{\partial\Sigma^\lambda}{\partial v}\frac{\partial\Sigma^\kappa}{\partial w}dudvdw, \tag{C2}$$

where $\epsilon_{\mu\nu\lambda\kappa}$ is the Levi-Civita symbol.

For example, in Cartesian coordinates the hypersurface normal vector is $\Sigma_\mu^{(t,z)}(t,x,y,z)$, where $t = t(x,y,z)$; hence

$$\begin{aligned} d^3\Sigma_\mu^{(t,z)} &\equiv (dxdydz, -dtdydz, -dtdxdz, -dtdxdy) \\ &= \tau\left(\frac{\partial\tau}{\tau\partial\eta}\sinh\eta + \cosh\eta, -\frac{\partial\tau}{\partial x}, -\frac{\partial\tau}{\partial y},\right. \\ &\quad \left. -\frac{\partial\tau}{\tau\partial\eta}\cosh\eta - \sinh\eta\right)dxdyd\eta, \end{aligned} \tag{C3}$$

while in (τ,x,y,η) coordinates for $\Sigma_\mu^{(\tau,\eta)}(\tau,x,y,\eta)$ and $\tau = \tau(x,y,\eta)$ we obtain

$$d^3\Sigma_\mu^{(\tau,\eta)} = \tau(dxdyd\eta, -d\tau dyd\eta, -d\tau dxd\eta, -d\tau dxdy). \tag{C4}$$

If we are interested in the conserved current across constant time or proper time hypersurfaces then $d^3\Sigma_i^{(t,z)} = d^3\Sigma_i^{(\tau,\eta)} = 0$; hence in Cartesian coordinates we get

$$N_{\rm tot}(t) \equiv \int N^\mu d^3\Sigma_\mu^{(t,z)} = \gamma n_0 \int dxdydz, \tag{C5}$$

where $N^\mu \equiv n_0 u^\mu = \gamma n_0(1, v_x, v_y, v_z)$ is the conserved charge current. Similarly, Eq. (C1) leads to the total conserved charge at any proper-time hypersurface in hyperbolic coordinates,

$$N_{\rm tot}(\tau) \equiv \int N^\mu d^3\Sigma_\mu^{(\tau,\eta)} = \gamma n_0 \int \tau dxdyd\eta. \tag{C6}$$

To calculate how the total energy-momentum changes between two closed hypersurfaces, first we define the energy-momentum current across a hypersuface as

$$E_{\rm tot}^\mu \equiv \int T^{\mu\nu} d^3\Sigma_\nu = \int T^{\mu 0} d^3\Sigma_0 + \int T^{\mu i} d^3\Sigma_i. \tag{C7}$$

In Cartesian coordinates $E_{\rm tot}^\mu = (E_{\rm tot}^0, E_{\rm tot}^i)$, such that $E_{\rm tot}^0$ denotes the energy current while $E_{\rm tot}^i$ denotes the momentum current trough the hypersurface. Therefore the total energy current across a constant-t hypersurface is

$$E_{\rm tot}^0(t) \equiv \int T^{0\nu} d^3\Sigma_\nu^{(t,z)} = \int T^{00} dxdydz. \tag{C8}$$

The energy-momentum current across a constant-τ hypersurface in (τ,x,y,η) coordinates can also be calculated from Eq. (C7) together with the general transformation rules $E_{\rm tot}^\mu = (\partial x^\mu/\partial\hat{x}^\alpha)\,\hat{E}_{\rm tot}^\alpha$, where the position vectors are $x^\mu \equiv (t,x,y,z) = (\tau\cosh\eta, x, y, \tau\sinh\eta)$ and $\hat{x}^\mu \equiv (\tau,x,y,\eta)$. Thus the total energy across a constant-τ hypersurface is given by

$$\begin{aligned} E_{\rm tot}^0(\tau) &\equiv \int \cosh\eta\; T^{\tau\nu} d^3\Sigma_\nu^{(\tau,\eta)} + \int \tau\sinh\eta\; T^{\eta\nu} d^3\Sigma_\nu^{(\tau,\eta)} \\ &= \int (\cosh\eta\; T^{\tau\tau} + \tau\sinh\eta\; T^{\eta\tau})\,\tau dxdyd\eta. \end{aligned} \tag{C9}$$

Using the latter formulas we can check energy conservation from the initial time to the end using

$$\Delta E_{\rm tot}^0(t) = E_{\rm tot}^0(t_{\rm end}) - E_{\rm tot}^0(t_{\rm ini}). \tag{C10}$$

It turns out that by solving the fluid dynamical equations in Cartesian coordinates we can achieve $\Delta E_{\rm tot}^0(t) \approx \mathcal{O}_6$

numerical accuracy, while in hyperbolic coordinates $\Delta E^0_{\rm tot}(\tau) \approx \mathcal{O}_1$. This behavior is due to two different reasons.

First, the numerical algorithm is accurate only to finite precision, meaning that T^{00} or $T^{\tau\tau}$ is calculated correctly only up to the first six digits. However, due to the hyperbolic functions in Eq. (C9) the total energy of the system is given by a differently weighted sum over all cells (compared to Cartesian coordinates). These hyperbolic weights increase very rapidly as a function of η; hence even though the numerical error of the solver is acceptably small for SHASTA, the weighted sum over all cells in hyperbolic coordinates shows otherwise.

We have checked that for RHIC energies $\Delta E^0_{\rm tot}(\tau) < 2\%$ while at LHC energies this number can be as much as 20%. This is because $f(\eta)$ is much narrower at the RHIC than at the LHC. Similar results were also obtained in Ref. [86] using a different computational fluid-dynamical algorithm.

We also verified energy conservation inside the constant-temperature freeze-out hypersurface, and we found that in that case the energy is conserved at 1% accuracy, at both the RHIC and the LHC. This was expected since inside the $T = 100$ MeV freeze-out hypersurface the space-time rapidity of matter is $\eta < 10$.

[1] I. Arsene *et al.*, Nucl. Phys. A **757**, 1 (2005); B. B. Back *et al.*, *ibid.* **757**, 28 (2005); J. Adams *et al.*, *ibid.* **757**, 102 (2005); K. Adcox *et al.*, *ibid.* **757**, 184 (2005).

[2] U. W. Heinz and R. Snellings, Annu. Rev. Nucl. Part. Sci. **63**, 123 (2013).

[3] C. Gale, S. Jeon, and B. Schenke, Int. J. Mod. Phys. A **28**, 1340011 (2013).

[4] P. Huovinen, Int. J. Mod. Phys. E **22**, 1330029 (2013).

[5] G. Policastro, D. T. Son, and A. O. Starinets, Phys. Rev. Lett. **87**, 081601 (2001); P. K. Kovtun, D. T. Son, and A. O. Starinets, *ibid.* **94**, 111601 (2005).

[6] C. Gale, S. Jeon, B. Schenke, P. Tribedy, and R. Venugopalan, Phys. Rev. Lett. **110**, 012302 (2013).

[7] L. P. Csernai, J. I. Kapusta, and L. D. McLerran, Phys. Rev. Lett. **97**, 152303 (2006).

[8] G. S. Denicol, C. Gale, S. Jeon, and J. Noronha, Phys. Rev. C **88**, 064901 (2013).

[9] H. Song, S. A. Bass, and U. Heinz, Phys. Rev. C **83**, 054912 (2011); **87**, 019902 (2013).

[10] U. W. Heinz, J. Phys.: Conf. Ser. **455**, 012044 (2013).

[11] H. Niemi, G. S. Denicol, P. Huovinen, E. Molnár, and D. H. Rischke, Phys. Rev. Lett. **106**, 212302 (2011).

[12] H. Niemi, G. S. Denicol, P. Huovinen, E. Molnár, and D. H. Rischke, J. Phys. G **38**, 124050 (2011); Acta Phys. Polon. Suppl. **5**, 305 (2012).

[13] H. Niemi, G. S. Denicol, P. Huovinen, E. Molnár, and D. H. Rischke, Phys. Rev. C **86**, 014909 (2012).

[14] H. Niemi and G. S. Denicol, arXiv:1404.7327 [nucl-th].

[15] H. Holopainen and P. Huovinen, J. Phys.: Conf. Ser. **389**, 012018 (2012).

[16] H. Holopainen and P. Huovinen, J. Phys.: Conf. Ser. **509**, 012114 (2014).

[17] L. D. Landau and E. M. Lifshitz, *Fluid Dynamics*, 2nd ed. (Butterworth-Heinemann, London, 1987).

[18] C. Cercignani and G. M. Kremer, *The Relativisitic Boltzmann Equation: Theory and Applications* (Birkhäuser, New York, 2002).

[19] G. Torrieri, B. Tomasik, and I. Mishustin, Phys. Rev. C **77**, 034903 (2008).

[20] A. Monnai and T. Hirano, Phys. Rev. C **80**, 054906 (2009).

[21] H. Song and U. W. Heinz, Phys. Rev. C **81**, 024905 (2010).

[22] P. Bozek, Phys. Rev. C **85**, 034901 (2012).

[23] K. Dusling and T. Schäfer, Phys. Rev. C **85**, 044909 (2012).

[24] J. Noronha-Hostler, G. S. Denicol, J. Noronha, R. P. G. Andrade, and F. Grassi, Phys. Rev. C **88**, 044916 (2013).

[25] J. Noronha-Hostler, J. Noronha, and F. Grassi, Phys. Rev. C **90**, 034907 (2014).

[26] S. Borsanyi, Z. Fodor, S. D. Katz, S. Krieg, C. Ratti, and K. Szabo, J. High Energy Phys. 01 (2012) 138.

[27] A. Bazavov *et al.* (HotQCD Collaboration), Phys. Rev. D **86**, 034509 (2012).

[28] P. Huovinen, P. Petreczky, and C. Schmidt, Central Eur. J. Phys. **10**, 1385 (2012).

[29] I. Müller, Z. Phys. **198**, 329 (1967).

[30] I. Müller, Living Rev. Relativity **2**, 1 (1999).

[31] W. Israel and J. M. Stewart, Ann. Phys. (NY) **118**, 341 (1979).

[32] G. S. Denicol, H. Niemi, E. Molnár, and D. H. Rischke, Phys. Rev. D **85**, 114047 (2012).

[33] G. S. Denicol, E. Molnár, H. Niemi, and D. H. Rischke, Eur. Phys. J. A **48**, 170 (2012).

[34] E. Molnár, H. Niemi, G. S. Denicol, and D. H. Rischke, Phys. Rev. D **89**, 074010 (2014).

[35] L. P. Csernai, V. K. Magas, E. Molnár, A. Nyiri, and K. Tamosiunas, Eur. Phys. J. A **25**, 65 (2005); E. Molnár, L. P. Csernai, V. K. Magas, A. Nyiri, and K. Tamosiunas, Phys. Rev. C **74**, 024907 (2006); E. Molnár, L. P. Csernai, V. K. Magas, Z. I. Lazar, A. Nyiri, and K. Tamosiunas, J. Phys. G **34**, 1901 (2007).

[36] S. V. Akkelin, Y. Hama, I. A. Karpenko, and Y. M. Sinyukov, Phys. Rev. C **78**, 034906 (2008); I. A. Karpenko and Y. M. Sinyukov, *ibid.* **81**, 054903 (2010).

[37] F. Cooper and G. Frye, Phys. Rev. D **10**, 186 (1974).

[38] J. P. Bondorf, S. I. A. Garpman, and J. Zimanyi, Nucl. Phys. A **296**, 320 (1978).

[39] C. M. Hung and E. V. Shuryak, Phys. Rev. C **57**, 1891 (1998).

[40] K. J. Eskola, H. Niemi, and P. V. Ruuskanen, Phys. Rev. C **77**, 044907 (2008).

[41] P. Huovinen and P. Petreczky, Nucl. Phys. A **837**, 26 (2010).

[42] M. Cheng *et al.*, Phys. Rev. D **77**, 014511 (2008).

[43] A. Bazavov *et al.*, Phys. Rev. D **80**, 014504 (2009).

[44] H. Bebie, P. Gerber, J. L. Goity, and H. Leutwyler, Nucl. Phys. B **378**, 95 (1992).

[45] T. Hirano and K. Tsuda, Phys. Rev. C **66**, 054905 (2002).

[46] P. Huovinen, Eur. Phys. J. A **37**, 121 (2008).

[47] M. Luzum and H. Petersen, J. Phys. G **41**, 063102 (2014).

[48] L. Pang, Q. Wang, and X.-N. Wang, Phys. Rev. C **86**, 024911 (2012).

[49] M. L. Miller, K. Reygers, S. J. Sanders, and P. Steinberg, Annu. Rev. Nucl. Part. Sci. **57**, 205 (2007).

[50] B. Alver, M. Baker, C. Loizides, and P. Steinberg, arXiv:0805.4411 [nucl-ex].

[51] B. Abelev *et al.* (ALICE Collaboration), Phys. Rev. C **88**, 044909 (2013).
[52] B. Schenke, P. Tribedy, and R. Venugopalan, Phys. Rev. Lett. **108**, 252301 (2012); Phys. Rev. C **86**, 034908 (2012).
[53] R. Paatelainen, K. J. Eskola, H. Niemi, and K. Tuominen, Phys. Lett. B **731**, 126 (2014).
[54] T. Hirano, Phys. Rev. C **65**, 011901(R) (2001).
[55] C. Nonaka and S. A. Bass, Phys. Rev. C **75**, 014902 (2007).
[56] B. Schenke, S. Jeon, and C. Gale, Phys. Rev. C **82**, 014903 (2010).
[57] J. D. Bjorken, Phys. Rev. D **27**, 140 (1983).
[58] A. Adil and M. Gyulassy, Phys. Rev. C **72**, 034907 (2005).
[59] T. Hirano, P. Huovinen, K. Murase, and Y. Nara, Prog. Part. Nucl. Phys. **70**, 108 (2013).
[60] V. Vovchenko, D. Anchishkin, and L. P. Csernai, Phys. Rev. C **88**, 014901 (2013).
[61] A. Dumitru, E. Molnár, and Y. Nara, Phys. Rev. C **76**, 024910 (2007).
[62] H. Holopainen, H. Niemi, and K. J. Eskola, Phys. Rev. C **83**, 034901 (2011).
[63] B. B. Back *et al.* (PHOBOS Collaboration), Phys. Rev. Lett. **91**, 052303 (2003).
[64] S. S. Adler *et al.* (PHENIX Collaboration), Phys. Rev. C **69**, 034909 (2004).
[65] T. Hirano and M. Gyulassy, Nucl. Phys. A **769**, 71 (2006).
[66] Y. Bai, Ph.D. thesis, Nikhef and Utrecht University, Netherlands, 2007; A. Tang (STAR Collaboration), arXiv:0808.2144 [nucl-ex].
[67] B. B. Back *et al.* (PHOBOS Collaboration), Phys. Rev. C **72**, 051901 (2005).
[68] J. Adams *et al.* (STAR Collaboration), Phys. Rev. C **72**, 014904 (2005).
[69] T. Hirano, U. W. Heinz, D. Kharzeev, R. Lacey, and Y. Nara, Phys. Lett. B **636**, 299 (2006).
[70] B. Schenke, S. Jeon, and C. Gale, Phys. Rev. C **85**, 024901 (2012).
[71] B. H. Alver, C. Gombeaud, M. Luzum, and J.-Y. Ollitrault, Phys. Rev. C **82**, 034913 (2010).
[72] E. Abbas *et al.* (ALICE Collaboration), Phys. Lett. B **726**, 610 (2013).
[73] B. Abelev *et al.* (ALICE Collaboration), Phys. Rev. C **88**, 044910 (2013).
[74] V. Begun, W. Florkowski, and M. Rybczynski, Phys. Rev. C **90**, 014906 (2014).
[75] K. Aamodt *et al.* (ALICE Collaboration), Phys. Rev. Lett. **105**, 252302 (2010).
[76] P. F. Kolb, J. Sollfrank, and U. W. Heinz, Phys. Rev. C **62**, 054909 (2000).
[77] E. Molnár, H. Niemi, and D. H. Rischke, Eur. Phys. J. C **65**, 615 (2010).
[78] J. P. Boris and D. L. Book, J. Comput. Phys. A **11**, 38 (1973); D. L. Book, J. P. Boris, and K. Hain, *ibid.* **18**, 248 (1975).
[79] S. T. Zalesak, J. Comput. Phys. A **31**, 335 (1979).
[80] D. Kuzmin, R. Löhner, and S. Turek, *Flux-Corrected Transport: Principles, Algorithms, and Applications*, 2nd ed. (Springer, New York, 2012).
[81] A. Muronga, Phys. Rev. C **76**, 014909 (2007).
[82] E. Molnár, Eur. Phys. J. C **60**, 413 (2009).
[83] D. Kuzmin, M. Möller, and S. Turek, Comput. Methods Appl. Mech. Eng. **193**, 4915 (2004).
[84] P. Huovinen and H. Petersen, Eur. Phys. J. A **48**, 171 (2012).
[85] https://karman.physics.purdue.edu/OSCAR/
[86] I. Karpenko, P. Huovinen, and M. Bleicher, Comput. Phys. Commun. **185**, 3016 (2014).